

IMPROVED CONSTRAINTS ON THE GRAVITATIONAL LENS Q0957+561. II. STRONG LENSING

R. FADELY¹, C. R. KEETON¹, R. NAKAJIMA^{2,3}, AND G. M. BERNSTEIN²

Draft version May 23, 2022

ABSTRACT

We present a detailed strong lensing analysis of an HST/ACS legacy dataset for the first gravitational lens, Q0957+561. With deep imaging we identify 24 new strongly lensed features, which we use to constrain mass models. We model the stellar component of the lens galaxy using the observed luminosity distribution, and the dark matter halo using several different density profiles. We draw on the weak lensing analysis by Nakajima et al. (2009) to constrain the mass sheet and environmental terms in the lens potential. Adopting the well-measured time delay, we find $H_0 = 85_{-13}^{+14}$ km s⁻¹ Mpc⁻¹ (68% CL) using lensing constraints alone. The principal uncertainties in H_0 are tied to the stellar mass-to-light ratio (a variant of the radial profile degeneracy in lens models). Adding constraints from stellar population synthesis models, we obtain $H_0 = 79.3_{-8.5}^{+6.7}$ km s⁻¹ Mpc⁻¹ (68% CL). We infer that the lens galaxy has a rising rotation curve and a dark matter distribution with an inner core. Intriguingly, we find the quasar flux ratios predicted by our models to be inconsistent with existing radio measurements, suggesting the presence of substructure in the lens.

1. INTRODUCTION

Since its inception, strong gravitational lensing has been used to probe galaxy mass distributions in a way that complements photometric and dynamical studies. In systems with numerous lensed features, especially partial or full Einstein rings, lensing can provide a fairly detailed description of the lens galaxy mass distribution (e.g., Kochanek et al. 1989, 2001; Kochanek 1995; Lehár et al. 1996, 1997; Trotter et al. 2000; Koopmans et al. 2006; Gavazzi et al. 2008; Suyu et al. 2008, 2009). In systems with only a few lensed images, however, there may be significant systematic uncertainties in the lens mass distribution. For example, four-image lenses typically constrain the angular structure of the lens potential reasonably well (e.g., Keeton et al. 1997), but often cannot determine the radial profile because the images lie at similar distances from the center of the galaxy (e.g., Keeton & Kochanek 1997; Kochanek 2002). Two-image lenses are better able to probe the radial profile, but provide only poor constraints on the angular structure of the lens potential (Rusin et al. 2003). In addition, further complications may arise if the lens galaxy lies in a group or cluster of galaxies that significantly affect the lens potential (see Keeton & Zabludoff 2004).

These issues explain the challenges associated with modeling the first gravitational lens discovered, Q0957+561 (Walsh et al. 1979). The two lensed images of the background quasar provide limited constraints on a lens potential that is complicated by the presence of a cluster surrounding the main lens galaxy (e.g., Kochanek 1991). To move beyond simple two-image reconstructions, Gorenstein et al. (1988b) and Garrett et al. (1994) used VLBI observations to resolve the radio structure of the quasars; but Grogin & Narayan (1996) and Barkana et al. (1999) found that the new radio constraints still could not strongly constrain the lens potential. Seeking yet more constraints, Bernstein et al. (1997) and Keeton et al.

(2000) used the Hubble Space Telescope to discover lensed images of the quasar host galaxy, but even they found that a range of models could reproduce all the strong lensing data (also see Bernstein & Fischer 1999). There were parallel efforts to obtain other kinds of data to provide independent constraints on the lens galaxy and cluster. Tonry & Franx (1997) measured the central velocity dispersion of the lens galaxy, which Romanowsky & Kochanek (1999) used in stellar dynamical models. Fischer et al. (1997) studied weak lensing by the cluster. Chartas et al. (2002) used the Chandra X-ray Observatory to detect the hot intracluster gas and estimate the cluster mass. Despite the growing amount of data for this system, a definitive description of the mass distribution has remained elusive.

Uncertainties in the mass distribution propagate into attempts to use the lens time delay to determine the Hubble constant, H_0 . In principle, lens time delays offer a simple measurement of the Hubble constant at cosmological distances that bypasses the distance ladder. In practice, however, H_0 is degenerate with certain aspects of the mass model (Falco et al. 1985; Gorenstein et al. 1988a; Williams & Saha 2000; Kochanek 2002; Saha & Williams 2006). Due to these degeneracies, measurements of H_0 in individual lens systems have yielded quite varied results. Figure 1 shows the lens systems for which individual modeling of the mass distribution has been done to determine H_0 . Examining the figure, it is unclear what value of H_0 such studies prefer. Roughly half of the previous studies are consistent with $H_0 < 60$ km s⁻¹ Mpc⁻¹, with most preferring $H_0 = 65\text{--}80$ km s⁻¹ Mpc⁻¹. Strikingly, only two studies, of Q0957+561 (Bernstein & Fischer 1999; Keeton et al. 2000) and PKS 1830-211 (Lidman et al. 1999), found H_0 values > 85 km s⁻¹ Mpc⁻¹.

In non-lensing studies, measurements of H_0 have reached better agreement. Using Cepheid variable stars as distance indicators, Freedman et al. (2001) obtained $H_0 = 72 \pm 2$ (stat.) ± 7 (syst.) km s⁻¹ Mpc⁻¹. Riess et al. (2009) recently analyzed a higher quality and more homogeneous sample of Cepheids and supernovae and found $H_0 = 74.2 \pm 3.6$ km s⁻¹ Mpc⁻¹. Results from measurements of the Cosmic Microwave Background (CMB) have given similar re-

¹ Department of Physics and Astronomy, Rutgers, The State University of New Jersey, Piscataway, NJ 08854; fadely@physics.rutgers.edu

² Department of Physics and Astronomy, University of Pennsylvania, Philadelphia, PA 19104; garyb@physics.upenn.edu

³ Space Sciences Laboratory, University of California, Berkeley, Berkeley, CA 94720; rnakajima@berkeley.edu

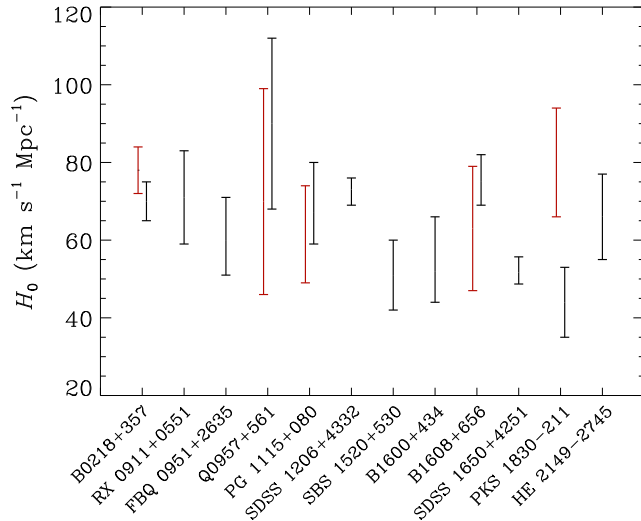


FIG. 1.— Current H_0 measurements in individual lens studies. Black errorbars indicate the most recent measurement for a given lens. When more than one such effort has been made, we present the second most recent effort in red. The measurements span a range of median values and uncertainties; a simple χ^2 test indicates the scatter is not purely statistical at $> 99\%$ confidence. *References*— B0218+357: Wucknitz et al. (2004); York et al. (2005), RX J0911+0551: Hjorth et al. (2002), FBQ0951+2635: Jakobsson et al. (2005), Q0957+561: Bernstein & Fischer (1999); Keeton et al. (2000), PG 1115+080: Treu & Koopmans (2002); Chartas et al. (2004), SDSS 1206+4332: Paraficz et al. (2009), SBS 1520+530: Burud et al. (2002b), B1600+434: Koopmans et al. (2000); Burud et al. (2000), B1608+656: Fassnacht et al. (2002); Koopmans et al. (2003), SDSS 1650+4251: Vuissoz et al. (2007), PKS 1830-211: Lidman et al. (1999); Winn et al. (2002), HE 2149-2745: Burud et al. (2002a).

sults. Most recently, Dunkley et al. (2008) analyzed the 5th year data release of the Wilkinson Microwave Anisotropy Probe (WMAP) to find $H_0 = 71.9^{+2.6}_{-2.7}$ km s $^{-1}$ Mpc $^{-1}$, assuming a universe with a flat geometry and a cosmological constant. With joint analyses of the various constraints, measurements of H_0 can now approach the percent level. For instance, Komatsu et al. (2008) combined H_0 measurements from the CMB, SNIa, and Baryon Acoustic Oscillations (BAO) to obtain $H_0 = 70.5 \pm 1.3$ km s $^{-1}$ Mpc $^{-1}$ or a 2.3% determination of H_0 .

Given the apparent consensus in non-lensing studies of H_0 , the scatter in results from lensing is puzzling. Are conventional lens models failing to account for variations in key components of lens models, such as the logarithmic density slope, angular structure, and/or substructure? Are the (often large) uncertainties in lensing measurements of H_0 fully understood? How can the uncertainties be reduced?

One way to confront these concerns is to model a statistical ensemble of lenses when measuring H_0 . Saha & Williams (2006) used non-parametric lens modeling to generate free-form mass maps of 10 lenses and obtain $H_0 = 72.5^{+7.8}_{-11.3}$ km s $^{-1}$ Mpc $^{-1}$. Adding one lens to this sample, Coles (2008) used similar techniques and found $H_0 = 71^{+6}_{-8}$ km s $^{-1}$ Mpc $^{-1}$. Oguri (2007) took a parametric approach but attempted to incorporate a reasonable amount of complexity and scatter in the models; his analysis of 16 time delay lenses yielded $H_0 = 68 \pm 6$ (stat.) ± 8 (syst.) km s $^{-1}$ Mpc $^{-1}$.

While these results are enticing, the systematic uncertainties may still be underestimated and cannot be beaten down with sample size. In particular, lensing constraints on H_0 are known to be affected by the “mass-sheet degeneracy”: a uniform sheet of mass can be added to a lensing potential in a way that leaves the positions and brightnesses of the images unchanged but rescales the inferred Hubble constant (Falco et al. 1985; Gorenstein et al. 1988a). Groups and clusters surrounding lens galaxies or along the line of sight can act as mass sheets that bias lensing measurements of H_0 (Keeton & Zabludoff 2004). While there is considerable effort to characterize the local and line-of-sight environments of strong lenses (e.g., Fassnacht & Lubin 2002; Fassnacht et al. 2006, 2008; Momcheva et al. 2006; Williams et al. 2006; Auger et al. 2007), and Oguri (2007) attempted to account for the mass sheet in several lenses for which it is expected to be significant, it is still not clear whether the systematic uncertainties are fully understood.

In order to identify and control systematics, it seems that we still need to model individual lens systems in detail. One advantage of this approach is the ability to use additional sources of information, such as weak lensing (e.g., Fischer et al. 1997; Bernstein & Fischer 1999) or stellar dynamics (e.g., Grogin & Narayan 1996; Tonry & Franx 1997; Treu & Koopmans 2002; Barnabè & Koopmans 2007), to reduce the uncertainties inherent in strong lensing. With the four-image lens B1608+656 (Myers et al. 1995), for example, Suyu et al. (2008, 2009) demonstrate that lensing and velocity dispersion information can be combined to get a $\sim 7\%$ determination of H_0 , in which the modeling uncertainties are comparable to the uncertainties in the measured time delays themselves (Fassnacht et al. 2002). With Q0957, we have a system whose complicated lens potential not only presents certain challenges for measuring H_0 , but also bestows certain opportunities. In particular, the presence of the cluster around the lens galaxies offers a rare chance to do a weak lensing analysis of an *individual* strong lens system (as opposed to a stacked ensemble; e.g., Gavazzi et al. 2007; Lagattuta et al. 2009), which is key to breaking the mass sheet degeneracy and controlling that vital systematic uncertainty. Furthermore, there is now a rich variety of data available for Q0957, which enables a broad-based analysis. We therefore study Q0957 to investigate statistical and systematic uncertainties in lens models and H_0 . The strong lensing analysis presented here complements and draws upon the weak lensing analysis presented by Nakajima et al. (2009); both are based on the same new HST/ACS data. In this system extensive observational effort (e.g., Schild & Cholfin 1986; Kundic et al. 1997; Oscoz et al. 2001) has yielded a very precise time delay with an uncertainty of just $\sim 0.02\%$ (Colley et al. 2003). While we do not expect to achieve that level of precision in lens models, our goal is to see just how well we can do. We combine our new data with a number of independent constraints from previous observations as well as stellar population synthesis models, in order to obtain the most precise measurement of H_0 to date for Q0957.

In this paper we assume a flat universe with matter density $\Omega_M = 0.274$ and cosmological constant $\Omega_\Lambda = 0.726$, which is consistent with the 5-year WMAP+SN+BAO constraints from Komatsu et al. (2008).

2. OBSERVATIONS AND DATA ANALYSIS

2.1. Observations

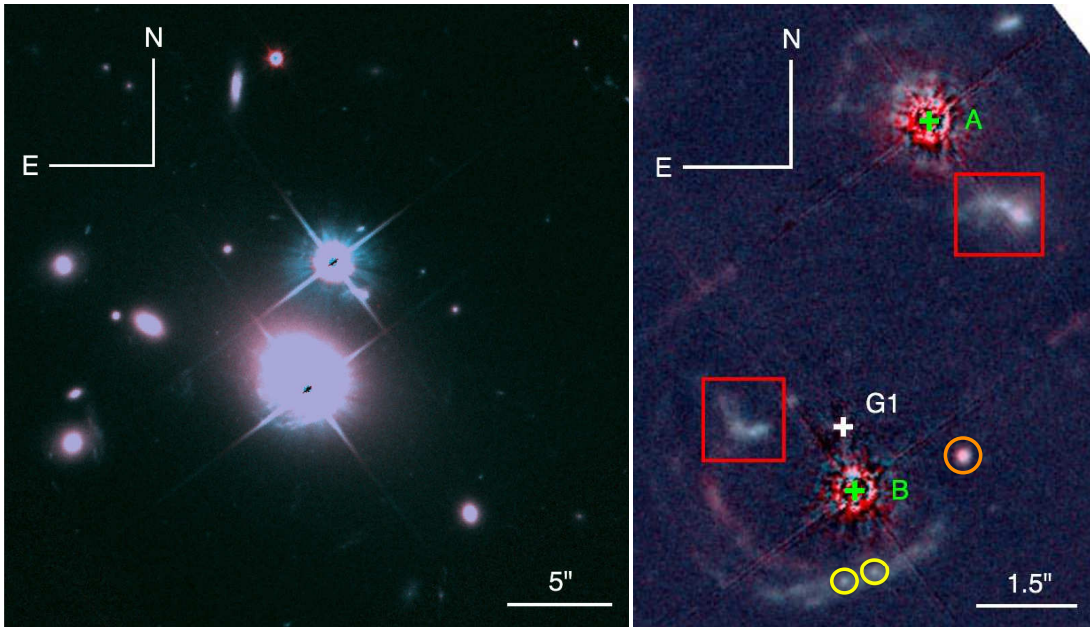


FIG. 2.— (a, left) A false color image of the central $30''$ of our combined F606W and F814W images of Q0957+561. (b, right) Close-up of the strong lensing region, after the main lensing galaxy and quasar images have been subtracted. The white cross indicates the center of the lens galaxy G1, while the green crosses indicate the quasar positions A and B. The red boxes and yellow circles indicate the “blobs” and “knots” identified by Bernstein et al. (1997). Newly resolved faint features are seen south and east around quasar B and southwest of quasar A. The orange circle indicates an unknown object, not associated with any lensed features. Since the light profile of the object is consistent with the PSF, we surmise it is a faint halo star in the foreground of the lens.

We conducted deep observations of Q0957+561 on 2005 October 10–11 with HST’s Advanced Camera for Surveys as part of program GO-10569. Using four pointings of 7.7 ks in the F606W filter and 3.8 ks in the F814W filter, we created a $6' \times 6'$ mosaic of the field. We arranged the pointings to overlap in the central $30''$ region, forming a 30 ks image in the F606W filter (15 ks in F814W) for our strong lensing analysis with a final pixel scale of $0.03''$. The large number of exposures in this central region allows us to use a simple image-combining algorithm that avoids the undesirable PSF broadening and noise correlation of the common *Drizzle* algorithm (Fruchter & Hook 2002):

1. An astrometric solution is derived for each exposure by compounding the ACS/WFC coordinate map of Anderson (2002) with an additional affine transformation to account for pointing errors, stellar aberration, and slight plate-scale variations due to the HST “breathing mode.” The coefficients of the affine transformation are derived by registering objects detected in individual exposures.
2. A grid of $0.03''$ pixels is created for the combined image. Each pixel in each exposure is mapped to a single destination pixel. Input pixels flagged as invalid due to detector defects, etc., are discarded.
3. For each destination pixel, we average all of the input pixels, using a sigma-clipping algorithm to eliminate pixels contaminated by cosmic rays.

The procedure is identical to the use of *Drizzle* with a “drop zone” of zero size. Since each input pixel contributes to only one output pixel, the output pixels have uncorrelated noise. The combining algorithm broadens the PSF only by an effective convolution with the output pixel square. The final pixel size is chosen such that it is small enough not to degrade the resolution, but coarse enough that there are enough input pixels for averaging and outlier rejection. We present a false

color image of our combined F606W and F814W images in Figure 2a.

To look for new strong lensing constraints, we subtract the bright quasar images A and B using the PSF derived from observations of the star HD237859. Since the PSF varies with focal plane position as well as time, we observed the star as close as possible in time and chip position to each quasar image in each of the four pointings.

2.2. Lens Galaxy Properties

We model the main lensing galaxy using the IRAF ELLIPSE task, masking out regions where quasar subtraction takes place as well as any bright regions not associated with the galaxy (e.g., other lensed features). Our resulting IRAF model provides a measurement of the galaxy’s isophotes and total flux (see Table 1). As shown previously (Bernstein et al. 1997), the isophotes of the lens galaxy exhibit an ellipticity gradient and a position angle twist (Figure 3). These isophotal features may complicate the lensing potential, so we incorporate them directly into our lens models (§3.2). We also use the photometry of the lens galaxy to constrain stellar population synthesis models and estimate the stellar mass-to-light ratio (§4.3).

2.3. Faint Strong Lensing Features

We subtract the model galaxy from the quasar-subtracted image to produce the final image of the strong lensing region, which is shown in Figure 2b. This image reveals several new, previously unresolved or undetected strongly lensed features. Since the morphology is similar to the host galaxy arc from NICMOS (Keeton et al. 2000), we conjecture that the optical features are most likely images of star forming regions of the quasar host galaxy at $z = 1.41$.

The lensed “blobs” and “knots” indicated in Figure 2b were previously identified by Bernstein et al. (1997), and were used by Bernstein & Fischer (1999) and Keeton et al. (2000) as

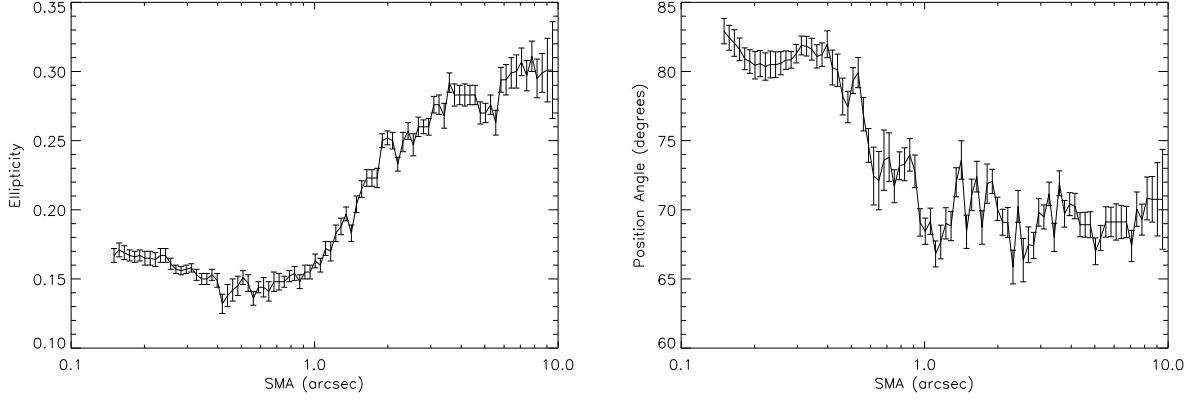


FIG. 3.— Ellipticity and position angle of galaxy isophotes, plotted as a function of semi-major axis. Note the increase in ellipticity beginning at $\sim 1''$ and the decrease in position angle beginning at $\sim 0.3''$.

constraints on lens models. To derive new constraints from our new strongly lensed features, we use the models of Keeton et al. (2000) as a starting point. Using the *lensmodel* software (Keeton 2001), we check to see how these older models would map new features in the image plane. Specifically, we take an observed image position, map it to the source plane, and then find all corresponding images using the old lens models. We then look for the predicted images in our new HST data. Unfortunately, we find the Keeton et al. models cannot sensibly reproduce the lensing we see in the HST data. These models fail most notably for the new features south and east of quasar B, mapping bright peaks in the data to blank regions of the sky.

In order to make sense of the new features, we examine the morphology of the images in the data. Specifically, in the area around the bright “knots” shown in Figure 2b we notice a distinct fork-like feature extending from either side of the knots. Using peaks in this structure, we postulate a set of new constraints as shown in the left panel of Figure 4, which we call our “primary” set of new constraints. We use these primary features to constrain a singular isothermal ellipsoid lens model, and see how the resulting model maps other faint features found in the HST data. Specifically, we consider faint features to the east of quasar B, indicated by the large box in Figure 4a. To our surprise, the model derived from our primary features accurately describes the remaining faint features, mapping peaks of the images in reasonable ways (Figure 4b) and giving us confidence in the identification of new lensed features. We therefore add these features to our list of constraints, resulting in a final data set which is given in Table 2. We note that all presumed multiple images of each source are observed to have similar colors (within the photometric noise).

To obtain the position and uncertainty of each peak listed in Table 2, we examine the brightest pixel(s) within the peak. If the brightest pixel is more than $10\sigma_{noise}$ above any other pixel in the peak (as for the “knots” or source IV in Table 2), we set the position error to be ± 1 pixel or $\pm 0.03''$. If the brightest pixel is $3-10\sigma_{noise}$ above the surrounding pixels, we conservatively set the error to ± 1.5 pixels or $\pm 0.05''$. If there are multiple pixels in the peak that are within $3\sigma_{noise}$ of the brightest, we take the average position of all such pixels and set the error to be the distance from this average to the farthest of the bright pixels, plus our nominal value of $0.05''$.

3. LENS MODELING METHODS

3.1. General Theory

In this section we present a brief review of the lensing theory that is particularly pertinent to our analysis of Q0957. For further discussion of strong lensing theory, please see Schneider et al. (1992) and Kochanek (2004).

As predicted by Einstein’s General Relativity in the early 20th century, a mass concentration near the line of sight to a background object may significantly displace and distort a background image. The angular position u of the source and the angular position of x of an image are related by the lens equation,

$$u = x - \nabla\phi, \quad (1)$$

where ϕ is the (scaled) gravitational potential due to mass at the lens redshift. The lens potential is given by

$$\nabla^2\phi(x) = 2\kappa(x) = 2\Sigma/\Sigma_{crit}, \quad (2)$$

where the convergence κ equals the surface mass density (Σ) scaled by the critical density for lensing (Σ_{crit}).

Since the deflected light travels along different ray paths, there is a difference in the light travel time for different images. This difference, known as the time delay, can be measured if the source is sufficiently variable. The time delay between images at positions x_i and x_j is given by

$$\Delta t_{ij} = \frac{1+z_l}{c} \frac{D_{ol}D_{os}}{D_{ls}} \times \left\{ \frac{1}{2} (|x_i - u|^2 - |x_j - u|^2) - [\phi(x_i) - \phi(x_j)] \right\}, \quad (3)$$

where z_l is the lens redshift and D_{ol} , D_{os} , and D_{ls} are angular-diameter distances from the observer to the lens, the observer to the source, and the lens to the source respectively. Combining a measured time delay with a lens model (to infer the source position u and the lens potential ϕ) provides a measurement of the distance combination $D_{ol}D_{os}/D_{ls}$, which is inversely proportional to H_0 . (The distance ratio also depends on cosmological parameters Ω_M and Ω_Λ , but that is typically a small effect compared with other uncertainties in the problem.)

A well-known problem in lensing constraints on H_0 is the “mass-sheet degeneracy” (Falco et al. 1985; Gorenstein et al. 1988a). For any potential ϕ that fits the data, one can construct

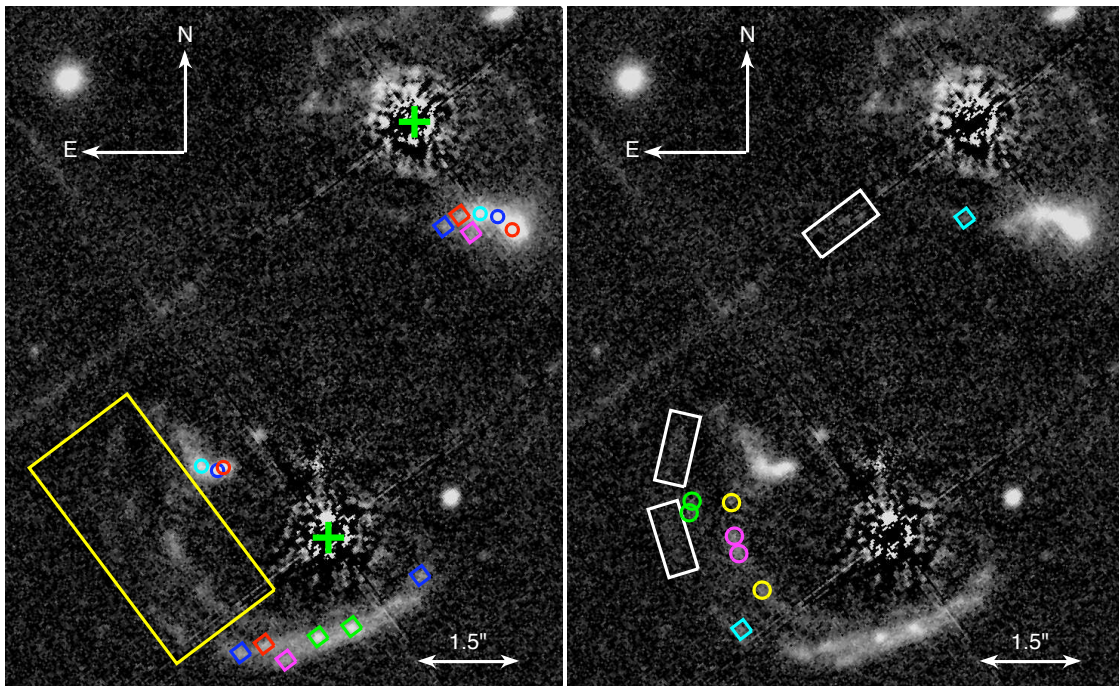


FIG. 4.— Our proposed mapping of the new lensed features (cf. Table 2). Corresponding shapes and colors indicate proposed images of a given source. The grid-like pattern that appears is due to the imperfect subtraction of the diffraction pattern of the quasar images. (a, left) We use the images indicated to constrain new lens models, and then use those models to test features in the yellow box. (b, right) We take one of the points in each shape/color pair, map it back to the image, and then find the corresponding images. The predicted positions match very well with features in the image, which gives us confidence both that the “primary” constraints are valid and that the additional lensed features are real. (Points in white rectangles indicate features that are too close to the noise level to provide confident peaks.) All of the colored points are used as constraints in our subsequent modeling.

another potential

$$\phi' = \frac{1}{2}\kappa'|x|^2 + (1-\kappa')\phi \quad (4)$$

that yields exactly the same image positions and flux ratios. The addition of the mass sheet κ' does, however, rescale the time delays and hence the inferred Hubble constant, such that $H'_0 = (1-\kappa')H_0$. The challenge for Q0957 is that the cluster around the lens contributes a term (κ_c in eq. 11 below) that acts like a mass sheet, which we cannot constrain by fitting the positions and fluxes of the strongly lensed images. We therefore set $\kappa_c = 0$ when doing the strong lens modeling, so we obtain some Hubble constant estimate $H_{0,model}$. We then use weak lensing data to constrain κ_c , which yields our corrected Hubble constant estimate

$$H_0 = (1-\kappa_c)H_{0,model}. \quad (5)$$

Additionally, since the mass sheet correction is a rescaling of the potential, we must multiply each term in the potential by the same factor of $1-\kappa_c$ as in eq. (5). For our results in §4, we indicate all parameters to which this applies.

3.2. Mass Models

3.2.1. Stellar component

The lensing potential of Q0957+561 may be complicated by the ellipticity gradient and isophote twist seen in the luminous component of the lens galaxy (see Figure 3). To allow such features in lens models, Keeton et al. (2000) introduced “double pseudo-Jaffe” models featuring a superposition of two ellipsoidal mass distributions, centered on the galaxy position, with different ellipticities, orientations, and scale radii. We initially adopted similar models, but quickly judged them to be unsatisfactory. Constrained by the new lensed features,

double pseudo-Jaffe models were adopting odd forms, such as one round and one very flattened component, that seemed unrealistic and unlike what is observed for giant elliptical galaxies.

A better approach is to incorporate the observed ellipticity gradient and isophote twist directly by using our isophotal model of the stellar component. We combine the model galaxy with an assumed stellar mass-to-light ratio to construct a convergence map. (We vary the mass-to-light ratio during the modeling, as discussed in §3.4.) To compute the corresponding lensing potential, we solve the Poisson equation using Fourier transforms. In Fourier space, the Poisson equation (2) has the form

$$-k^2 F(k) = 2K(k) \quad (6)$$

where $K(k)$ is the Fourier transform of the convergence map and $F(k)$ is the Fourier transform of the lens potential. It is straightforward to construct the convergence on a two-dimensional grid, calculate $K(k)$ using FFTs, solve for $F(k)$, and then do an inverse Fourier transform to get $\phi(x)$. We can then obtain the lensing deflection and magnification by computing derivatives of $\phi(x)$ in Fourier space. This method is discussed in more detail by van de Ven et al. (2009).

3.2.2. Dark matter

The luminous galaxy is presumably embedded in its own dark matter halo and any halo associated with the surrounding cluster. The cluster in Q0957 is non-negligible: previous weak lensing studies constrained the mean convergence within $30''$ of the lens to be $\kappa_{30''} = 0.26 \pm 0.16$ and indicated a shear of $\gamma \sim 0.2$ (Fischer et al. 1997; Bernstein & Fischer 1999). (In §3.5 we report our own constraints on cluster mass models.) Also, X-ray observations of the intracluster gas in-

indicated a convergence from the cluster at the quasar positions of $\kappa_A = 0.22^{+0.14}_{-0.07}$ and $\kappa_B = 0.21^{+0.12}_{-0.07}$ (Chartas et al. 2002).

Since the lens galaxy is the brightest and (presumably) most massive galaxy in the cluster, it seems natural to assume as a fiducial model that the galaxy lies at the center of the cluster. In this case the dark matter halo we insert in our models represents some combination of dark matter associated with the galaxy and dark matter associated with the cluster as a whole. We consider various profiles to encompass the range of possibilities. One model we use is the Navarro-Frenk-White profile (NFW, Navarro et al. 1997),

$$\rho = \frac{\rho_s}{(r/r_s)(1+r/r_s)^2} \quad (7)$$

whose projected surface density has the form (Bartelmann 1996)

$$\kappa(r) = 2\kappa_s \frac{1 - \mathcal{F}(x)}{x^2 - 1} \quad (8)$$

where $x = r/r_s$, $\kappa_s = \rho_s r_s / \Sigma_{crit}$, and

$$\mathcal{F}(x) = \begin{cases} \frac{1}{\sqrt{x^2-1}} \tan^{-1} \sqrt{x^2-1} & (x > 1) \\ \frac{1}{\sqrt{1-x^2}} \tanh^{-1} \sqrt{1-x^2} & (x < 1) \\ 1 & (x = 1) \end{cases} \quad (9)$$

While these equations describe a spherically symmetric model, we can obtain an elliptical model by replacing r with the ellipse coordinate $\xi = (x^2 + y^2/q^2)^{1/2}$ where q is the projected axis ratio. The lensing potential and its derivatives can be computed for elliptical models using numerical integrals (Schramm 1990; Keeton 2001).

We also use three softened power law profiles with projected surface densities of the form

$$\kappa(\xi) = \frac{1}{2} \frac{b_d^{2-\alpha}}{(a^2 + \xi^2)^{1-\alpha/2}} \quad (10)$$

where ξ is the ellipse coordinate defined above, a is the core radius, b_d is a normalization parameter, and the power law index α is chosen such that $M(R) \propto R^\alpha$ for $R \gg a$. In this class of models we study one with an isothermal profile ($\alpha = 1$), one steeper than isothermal ($\alpha = 0.5$), and one shallower than isothermal ($\alpha = 1.5$). For $\alpha = 1$ the lensing potential and its derivatives can be computed analytically (Keeton & Kochanek 1998), but for $\alpha \neq 1$ they require numerical integrals.

We still need to consider the possibility that the cluster may not be centered on the lens galaxy, which is germane because the observed X-ray emission from the cluster is slightly offset from the lens: the X-ray centroid is 4.3 ± 1.3 arcsec East and $3.2^{+1.2}_{-0.6}$ arcsec North of Image B, or 4.7 ± 1.2 arcsec from the lens galaxy (Chartas et al. 2002). We carry out our full modeling analysis (as described in the remainder of the paper) treating the cluster as a distinct dark matter halo centered at the observed X-ray position. While this approach yields fits that are formally comparable to our fiducial results, we ultimately reject such models for two reasons. When we treat the offset cluster with a softened power law profile, the models require a large ($> 30''$) core radius, which makes the ‘‘cluster’’ basically equivalent to a uniform mass sheet on the $\sim 6''$ scale of strong lensing and thus negates the effect of having an extra halo. NFW models cannot mimic that behavior, of course, since they do not have a flat core. Instead, we find

that an offset NFW cluster must have an unreasonably large ellipticity of > 0.7 . We conclude that the strong lens data do not favor and in fact disfavor an offset cluster, so we not include a separate cluster component in our main analysis.

3.2.3. Environmental terms

While our lens-centered mass profiles should account for the majority of the mass in the strong lensing region (apart from a mass sheet), they should not be expected to represent the full complexity of the cluster potential. The cluster halo may not be a simple ellipsoid on large scales, and it presumably has some lumpiness in the form of individual cluster galaxies. In general, we can write the lens potential due to structures outside the strong lensing region using a Taylor series expansion of the form

$$\phi_{env}(r, \theta) = \frac{\kappa_c}{2} r^2 + \frac{\gamma}{2} r^2 \cos 2(\theta - \theta_\gamma) + \frac{\sigma}{4} r^3 \cos(\theta - \theta_\sigma) + \frac{\delta}{6} r^3 \cos 3(\theta - \theta_\delta) + \dots \quad (11)$$

where κ_c is a mass sheet, γ is an external shear, and σ and δ represent higher, third-order terms. If the structures are ‘‘far’’ enough from the Einstein radius, the higher-order terms may be sufficiently small that the expansion can be truncated after the shear; indeed this approximation is used in many lens systems. However, as shown by Kochanek (1991) and many subsequent studies, the third-order terms cannot be neglected in Q0957. Bernstein & Fischer (1999) and Keeton et al. (2000) included the third-order terms but imposed the assumptions $\sigma = -2\delta/3$ and $\theta_\sigma = \theta_\delta$, which corresponds to the perturbation from a singular isothermal sphere. We find that this assumption is too restrictive, so we include general third-order terms in order to allow more freedom in the models to account for complex features we have not explicitly modeled.

Note that we have written eq. (11) in terms of the amplitudes (γ, σ, δ) and directions ($\theta_\gamma, \theta_\sigma, \theta_\delta$) of the shear and third-order terms. We can think of these as ‘‘polar’’ coordinate versions of these parameters. We can equivalently define ‘‘Cartesian’’ coordinate versions of the same parameters:

$$\begin{aligned} \gamma_c &= \gamma \cos 2\theta_\gamma, & \gamma_s &= \gamma \sin 2\theta_\gamma, \\ \sigma_c &= \sigma \cos \theta_\sigma, & \sigma_s &= \sigma \sin \theta_\sigma, \\ \delta_c &= \delta \cos 3\theta_\delta, & \delta_s &= \delta \sin 3\theta_\delta. \end{aligned} \quad (12)$$

While we quote results for the ‘‘polar’’ parameters, we actually carry out our modeling analysis using the ‘‘Cartesian’’ parameters. The translation is straightforward.

In summary, our composite models consist of a stellar component, an elliptical halo centered on the stellar component that accounts for dark matter in the lens galaxy and/or cluster halo, and an additional set of terms corresponding to a third-order Taylor series expansion of the potential from the lens environment. The 11 associated model parameters are listed in Table 3.

3.3. Model Constraints

Table 2 lists the positions of the lensed images used as constraints on our models. We supplement the faint images discussed in §2.3 with the quasar cores and radio jets resolved with Very Long Baseline Interferometry (VLBI; Gorenstein et al. 1988b; Garrett et al. 1994). With a resolution of ~ 0.1 mas, the VLBI observations reveal structure within the jets and provide astrometry with formal errors < 1 mas. Previous studies of Q0957 used this excellent astrometry as strong

constraints on lens models (Barkana et al. 1999; Bernstein et al. 1997; Bernstein & Fischer 1999; Keeton et al. 2000). In this work, however, we reconsider the use of such stringent constraints. Many recent works have shown that lens galaxies often contain substructure in the form of CDM subhalos, which can perturb lens flux ratios by tens of percent or more and image positions at levels up to ~ 10 mas (e.g., Mao & Schneider 1998; Metcalf & Madau 2001; Dalal & Kochanek 2002; Chiba et al. 2005; Chen et al. 2007). Since our models do not contain any substructure,⁴ they should not be expected to match the image positions to better than the ~ 10 mas residuals expected from substructure. We therefore broaden the errorbars and adopt conservative uncertainties on the VLBI quasar and jet positions of 30 mas. As a check, we verified that the VLBI derived positions of the quasars are in good agreement with the positions in our HST data.

We take the image position constraints together with constraints from our weak lensing analysis (§3.5) to comprise our main model constraints. Subsequently, we consider adding supplementary constraints in the form of lensed arcs detected with HST/NICMOS, the quasar radio flux ratio, and stellar population synthesis models (see §4 for details). Throughout the analysis we use the time delay 417.09 ± 0.07 days from Colley et al. (2003) to infer the Hubble constant.

3.4. Strong Lensing Analysis

In Bayesian language, our ultimate goal is to determine the posterior probability distribution for our model parameters and H_0 , given the observational constraints. We have $N_{data} = 60$ position constraints, compared with $N_{param} = 39$ free parameters (11 parameters for the mass model plus 28 source position parameters). Hence our analysis has $N_{data} - N_{param} = 21$ degrees of freedom. The Hubble constant analysis involves one additional constraint (the observed time delay) and one additional parameter (H_0), so it has the same number of degrees of freedom.

Formally, the posterior probability distribution has the form

$$P(\theta|d, M) = \frac{P(d|\theta, M)P(\theta|M)}{P(d|M)}, \quad (13)$$

where d denotes the data that provide constraints on the parameters θ associated with some model M . The likelihood of the data given the model is

$$\mathcal{L} \equiv P(d|\theta, M) \propto e^{-\chi^2/2}, \quad (14)$$

where χ^2 is the goodness of fit. The quantity $P(\theta|M)$ represents priors on the model parameters, which we take to be uniform.⁵ The Bayesian Evidence $P(d|M)$ is discussed below.

To ease the search of our large parameter space, we treat the image positions using the approximate position χ^2 as defined by Keeton (2001):

$$\chi_p^2 = \sum_i \delta x_i^T \cdot S_i^{-1} \cdot \delta x_i \approx \sum_i \delta u_i^T \cdot \mu_i^T \cdot S_i^{-1} \cdot \mu_i \cdot \delta u_i, \quad (15)$$

where the sum runs over all images, $\delta x_i = x_{obs,i} - x_{mod,i}$ is the position residual for image i , $S_i = \text{diag}(\sigma_i^2, \sigma_i^2)$ is the covariance matrix for the image positions, and μ_i is the lensing

⁴ It would certainly be interesting to add substructure to the models and use the precise radio positions and flux ratios to constrain the amount of substructure in the lens; but that is beyond the scope of the present work.

⁵ Note that our uniform priors apply to the ‘‘Cartesian’’ coordinate versions of the environmental parameters (eq. 12) and the ellipticity ($e_c = e \cos 2\theta_e$ and $e_s = e \sin 2\theta_e$).

magnification tensor. Using the lens equation, the position residual in the source plane is $\delta u_i = x_{obs,i} - \nabla\phi(x_{obs,i}) - u_{mod}$. The last step in eq. (15) is valid when the position residuals are small such that the image and source plane residuals are related by $\delta x_i \approx \mu_i \cdot \delta u_i$. The benefit of using this approach is that χ_p^2 is quadratic in each source position u_{mod} , so we can find the best-fit value analytically:

$$u_{mod} = A^{-1}b, \quad (16)$$

where

$$A = \sum_i \mu_i^T \cdot S_i^{-1} \cdot \mu_i, \quad (17)$$

$$b = \sum_i \mu_i^T \cdot S_i^{-1} \cdot \mu_i \cdot u_{obs,i}, \quad (18)$$

where these sums now run over the known images of a given source. The upshot is that we do not have to search explicitly through the 28 dimensions corresponding to the source parameters. An additional advantage is that we only have to compute the lens potential and its derivatives at the known positions of the images, which is useful for our dark matter models that require numerical integrals.

We must still search the 11-dimensional space of mass model parameters. We sample the posterior probability distribution in this space using an adaptive Metropolis-Hastings Monte Carlo Markov Chain (MCMC) algorithm (Roberts et al. 1997; Haario et al. 2001; Roberts & Rosenthal 2001). Each chain consists of a sequence of trial steps drawn from a multivariate Gaussian distribution. In 95% of the steps the Gaussian is based on an empirically updated covariance matrix to provide efficient sampling of a high-dimensional posterior distribution. In the remaining 5% of the steps the covariance matrix is diagonal so the algorithm takes independent and relatively large steps along the coordinate axes; this feature acts as a ‘‘fail-safe’’ to help the algorithm escape local minima in the χ^2 surface and potentially discover new features in the posterior distribution. The probability of accepting a trial step that modifies the likelihood from \mathcal{L}_{old} to \mathcal{L}_{new} is $\min(1, \mathcal{L}_{new}/\mathcal{L}_{old})$. In other words, if a trial step increases the likelihood it is automatically accepted; while if it decreases the likelihood it is accepted with a probability given by the likelihood ratio.

We run 25 chains simultaneously and set them up to work ‘‘from the outside in.’’ That is, we generate an initial sample of models by drawing $\sim 10^4$ random points in the parameter space and optimizing them; this provides an estimate of the allowed parameter ranges (although without the proper statistical sampling that MCMC provides). We then select models with maximal/minimal values of individual parameters to use as starting points for the MCMC chains. By starting with well spread chains, the MCMC algorithm can establish the covariance matrix more quickly, and spend more time sampling the tails of the distribution, than it would by starting with closely-spaced starting points (Gelman et al. 1995). The choice of initial models does not matter in detail, though, because for our final sampling we merge only the second halves of the chains in order to avoid sensitivity to the initial ‘‘burn-in’’ phase.

To assess whether an MCMC run has converged, we use the criterion presented by Gelman et al. (1995). For any given

parameter θ we define

$$R(\theta) = \left[\frac{\text{var}(\theta)}{\frac{1}{J} \sum_{j=1}^J \text{var}_j(\theta)} \right]^{1/2}, \quad (19)$$

where $\text{var}_j(\theta)$ is the variance of θ in the individual chain j , and $\text{var}(\theta)$ is the variance of θ over the entire set of J chains. Heuristically, R is a comparison of the variance of the entire distribution (the numerator) and the variance within individual chains (the denominator). The ratio will be greater than 1 for disjoint chains, and it will decrease and asymptotically approach 1 as the chains converge. Gelman et al. (1995) find that stopping an MCMC run once R reaches values below 1.2 provides a sufficient description of the target distribution for most samplings. To be conservative we run until $R \leq 1.1$ for every parameter. We then repeat the entire MCMC analysis a total of three times to obtain robust sampling of the target distribution.

In general we let all 11 model parameters vary simultaneously. The only exception is the scale radius in models with an NFW dark matter halo. There is a strong covariance between r_s and other parameters, which produces a narrow, curved ridge in the likelihood surface that is difficult for MCMC algorithms to sample efficiently. To deal with this challenge, we discretely sample r_s in logarithmic steps ranging from $0.1''$ to $1000''$. We checked that the median values of parameters in the posterior distributions do not vary more than 5% between steps. To combine results from individual r_s runs into the final posterior distribution, we need to normalize the individual results properly using eq. (13). In particular, we need to determine the normalization factor

$$P(d|M) = \int P(d|\theta, M) P(\theta|M) d\theta, \quad (20)$$

which is known as the marginal likelihood or Bayesian Evidence. Computing this integral usually requires techniques that are more computationally intensive than basic MCMC sampling, such as thermodynamic integration (e.g., Marshall et al. 2003; Lartillot & Phillippe 2006). However, it is possible to obtain a simple and useful surrogate for the evidence using the Bayesian Information Criterion,

$$\text{BIC} = -2 \ln \mathcal{L}_{\max} + k \ln N, \quad (21)$$

where \mathcal{L}_{\max} is the maximum likelihood of the model, k is the number of free parameters, and N is the number points used in the fit. While the BIC does not provide a proper statistical treatment of the evidence, it has been widely used in statistics and astronomy (e.g., Schwarz 1978; Rapetti et al. 2007; Davis et al. 2007; Liddle 2007) and is sufficient for this study.

As discussed in §4, we first examine models constrained only by the positions of the strongly lensed images, and then add supplemental constraints from weak lensing and various other considerations. In practice, this means we run the MCMC analysis to sample the likelihood eq. (14) based on the goodness of fit χ_p^2 from eq. (15). (Since we use uniform priors, the posterior probability distribution is proportional to the likelihood.) Now suppose we want to add some supplemental constraints characterized by their own goodness of fit χ_s^2 . The total χ^2 is just the sum $\chi_p^2 + \chi_s^2$ (i.e., χ^2 values add and likelihoods multiply), so we now want to sample

$$P(\theta|d, M) \propto e^{-\chi_s^2/2} e^{-\chi_p^2/2}. \quad (22)$$

Since the MCMC analysis provides a set of points drawn from $e^{-\chi_p^2/2}$, all we need to do is take those points and re-weight them by a factor proportional to $e^{-\chi_s^2/2}$. This provides a simple way to apply additional constraints without having to repeat the full MCMC analysis.

3.5. Weak Lensing Analysis

In parallel with the strong lensing analysis, we have conducted a weak lensing analysis of the full $6' \times 6'$ map to constrain the mass sheet and other environmental terms in the lensing potential (see eq. 11). The techniques and results of our weak lensing analysis are presented by Nakajima et al. (2009). We find the cluster potential to be consistent with a core-softened isothermal sphere profile, $\kappa(r) = \kappa_0 [1 + (r/r_c)^2]^{-1/2}$, with a best-fit central convergence $\kappa_0 = 0.47 \pm 0.17$ for a core radius $r_c = 5.0''$, corresponding to a velocity dispersion of $(420 \pm 70) \text{ km s}^{-1}$ for $h = 0.70$. Additionally, we find the cluster to be consistent with an NFW profile but are unable to provide useful constraints on the cluster concentration and scale radius.

One product of our weak lensing analysis is the average convergence within $30''$ of the lens: $\kappa_{w,30''} = 0.166 \pm 0.056$. This represents the net convergence including contributions from both the lens galaxy and the cluster. As discussed in §3.1, to determine the Hubble constant we need to know the correction from the cluster mass sheet,

$$1 - \kappa_c = \frac{1 - \kappa_{w,30''}}{1 - \kappa_{s,30''}} \quad (23)$$

where $\kappa_{w,30''}$ is the net convergence inside $30''$ from our weak lensing measurement while $\kappa_{s,30''}$ is the contribution from our strong lensing model. Since we do not impose *a priori* limits on $\kappa_{s,30''}$ in our models, the possibility exists that $\kappa_{s,30''}$ could exceed $\kappa_{w,30''}$. In this sense, our measurement of $\kappa_{w,30''}$ provides an upper bound on strong lens models. We penalize models with $\kappa_{s,30''} > \kappa_{w,30''}$ by adding an additional χ^2 term of the form

$$\chi_{\kappa}^2 = \begin{cases} \frac{(\kappa_{s,30''} - \kappa_{w,30''})^2}{\sigma_{\kappa_{w,30''}}^2}, & \kappa_{s,30''} > \kappa_{w,30''} \\ 0, & \kappa_{s,30''} < \kappa_{w,30''} \end{cases} \quad (24)$$

When we apply the mass sheet correction to H_0 and mass model parameters, we need to account for the measurement uncertainties in $\kappa_{w,30''}$. We do this using Monte Carlo techniques. Specifically, we take each model from our MCMC runs and generate a distribution of values for $1 - \kappa_c$ by drawing from a Gaussian distribution for $\kappa_{w,30''}$ set by the measurement and uncertainty from our weak lensing analysis. (The factor of $\kappa_{s,30''}$ in eq. 23 comes from the model itself.) We then fold this distribution into our final results reported in §§4.1–4.4.

The weak lensing analysis also yields constraints on the average shear in an annulus centered on the lens galaxy extending from $20''$ to $40''$: the two ‘‘Cartesian’’ shear components are $\gamma_c = -0.009 \pm 0.045$ and $\gamma_s = 0.092 \pm 0.045$, or equivalently the two ‘‘polar’’ components are $\gamma = 0.093 \pm 0.045$ and $\theta_\gamma = 47.8 \pm 13.9 \text{ deg}$.⁶ To compare this measurement to our models, we calculate the mean shear in the same annulus. After multiplying our value of the mean shear by the $1 - \kappa_c$

⁶ Note that the uncertainties are likely to be non-Gaussian for the ‘‘polar’’ components.

correction, we impose the weak lensing results as constraints on the lens models through additional χ^2 terms. These constraints penalize models with unusually small or large shears.

4. RESULTS

We first present results from lens models based on our new HST/ACS data (§4.1). We then consider adding additional constraints from the quasar radio flux ratio (§4.2), stellar population synthesis models (§4.3), and physical properties of NFW halos (§4.4). All values we report for the parameters (Υ_{F606W} , b_d , γ , σ , δ), as well as the dimensionless Hubble constant $h = H_0/(100 \text{ km s}^{-1} \text{ Mpc}^{-1})$, are corrected for the mass sheet through the factor $1 - \kappa_c$ (including the associated uncertainties; see §3.5).

4.1. Basic Results: Strong and Weak Lensing

For each of the four dark matter profiles we consider, we find a wide range of models that fit the HST strong lensing data well ($\chi^2_{reduced} < 1$).⁷ For example, the stellar mass-to-light ratio can be anywhere in the range $\Upsilon_{F606W} \sim 4\text{--}12$, the ellipticity $e \sim 0.1\text{--}0.7$, and shear $\gamma \sim 0.04\text{--}0.12$. Table 5 lists the median value and 68% and 95% confidence intervals for each model parameter (from the individual marginalized posterior probability distributions). The Table also lists the relative probabilities of our four dark matter models obtained by integrating the posterior probability distributions over h , after weighting by the BIC. The range of allowed models is striking given that we now have so many strong lensing constraints. Examining the relative probabilities, we find an isothermal ($\alpha = 1$) dark matter profile is favored from lensing alone. It is interesting to note, however, that our isothermal models require a values of $\kappa_{s,30'}$ which are larger than, but still consistent with our weak lensing measurements.

There are various ways to examine the results, so let us begin with the Hubble constant. Figures 5–8 show the marginalized joint probability distributions $P(\theta, h)$ for each model parameter θ and the dimensionless Hubble constant h , for all four classes of dark matter models. Viewing the results this way helps reveal any important degeneracies or systematics that affect the inferred value of h . The most obvious feature is a strong degeneracy between h and the stellar mass-to-light ratio, Υ_{F606W} , which we discuss momentarily. Focusing on h itself, Figure 9 shows the marginalized cumulative posterior probability distribution for h from each of our dark matter models. Combining the four models (weighted by their relative probabilities), we find $H_0 = 85^{+14}_{-13} \text{ km s}^{-1} \text{ Mpc}^{-1}$ (68% CL). Our measurement of H_0 is somewhat higher than, but statistically consistent with, the recent determinations of $H_0 = 74.2 \pm 3.6 \text{ km s}^{-1} \text{ Mpc}^{-1}$ from SNe (Riess et al. 2009) and $H_0 = 70.5 \pm 1.3 \text{ km s}^{-1} \text{ Mpc}^{-1}$ from WMAP5+BAO+SNe (Komatsu et al. 2008). Compared with previous results from Q0957 (Bernstein & Fischer 1999; Keeton et al. 2000), our initial results have lowered the median⁸ value from ~ 90 to 85 and reduced the spread by $\sim 30\%$. The latter result is significant given the new complexity in our models, the relaxation of (previously tight) quasar and jet positions, and the elimination of the quasar flux ratio constraint.

⁷ As shown in Table 5, the best-fit model in each model class has a reduced χ^2 somewhat less than unity. We used the χ^2 probability distribution to check that these values are statistically reasonable given the numbers of degrees of freedom.

⁸ The old median value for H_0 is not very well determined, because the previous analyses did not include the proper statistical sampling provided by our MCMC analysis.

The degeneracy between h and the stellar mass-to-light ratio Υ_{F606W} arises because the total mass within the Einstein radius is fixed, so varying Υ_{F606W} changes the balance between the concentrated stellar component and the more diffuse dark matter halo. That, in turn, modifies the slope of the total density profile, which is known to be the main factor that determines h (e.g., Williams & Saha 2000; Kochanek 2002). To illustrate these effects, we examine the monopole deflection curve, $\alpha(r) \propto M(r)/r$ where $M(r)$ is the projected mass within radius r (e.g., Blandford & Narayan 1986; Blandford & Kochanek 1987; Cohn et al. 2001; Kochanek et al. 2006; van de Ven et al. 2009). This is a 2D analog of the rotation curve. A flat deflection curve corresponds to an isothermal profile, while a rising (falling) curve corresponds to a profile shallower (steeper) than isothermal. Figure 10 shows the deflection curves for models with different values of h . There is a systematic change in the slope of the deflection curve with h , with very little ($< 2\%$) scatter among models at a fixed value of h . In other words, even though Q0957 has a complex lens potential, we still recover the familiar result that the slope of the total density profile is what principally determines h . In our models, the slope of the density profile is governed by the stellar mass-to-light ratio, which makes Υ_{F606W} the key parameter responsible for the range of h values. We consider external constraints on Υ_{F606W} in §4.3 below.

One interesting aspect of Figure 10 is that Q0957 appears to have a rising deflection curve, corresponding to a total density profile that is shallower than isothermal, for any reasonable value of h . Many other lens galaxies have profiles that are closer to isothermal (e.g., Cohn et al. 2001; Rusin & Kochanek 2005; Koopmans et al. 2006). Q0957 is not, however, unique in this regard: Kochanek et al. (2006) found that HE 0435–1223 also has a rising deflection curve. They argue that different density profiles and deflection curves can arise as a consequence of how galaxies populate dark matter halos. In the halo model (see Cooray & Sheth 2002 for a review), a group or cluster of galaxies consists of a massive central galaxy surrounded by smaller satellite galaxies. Lying as it does at the center of the potential well, the central galaxy should have a higher dark matter surface density compared to its satellite neighbors, which would lead to a more diffuse mass distribution with a shallower profile and hence a rising deflection curve. In this context, Kochanek et al. (2006) argue that HE0435 may be the central galaxy in a group of galaxies. Q0957 seems to fit naturally into this picture because it lies at or near the center of a modest cluster of galaxies (see §3.2).

One useful way to characterize a strong lens system is with the lensing critical curves and caustics. The critical curves reveal highly magnified regions in the image plane, and the corresponding caustics separate regions in the source plane that lead to different numbers of lensed images. Figure 11 shows examples of the critical curves for our models of Q0957. It is clear that the newly identified HST/ACS features have tightly constrained where the critical curve lies, especially southeast of quasar B. Significant variations do still exist near the ends of the critical curves, suggesting that constraints from the faint, unused features indicated in Figure 4 could help to further constrain the critical curves and restrict the parameter space. Unfortunately, in the current data these features have a signal to noise ratio less than 3, making them not sufficiently reliable.

In addition to Υ_{F606W} , our models exhibit a second degeneracy between h and the ellipticity of the dark matter halo. While the exact origin of this is unclear, it is likely connected

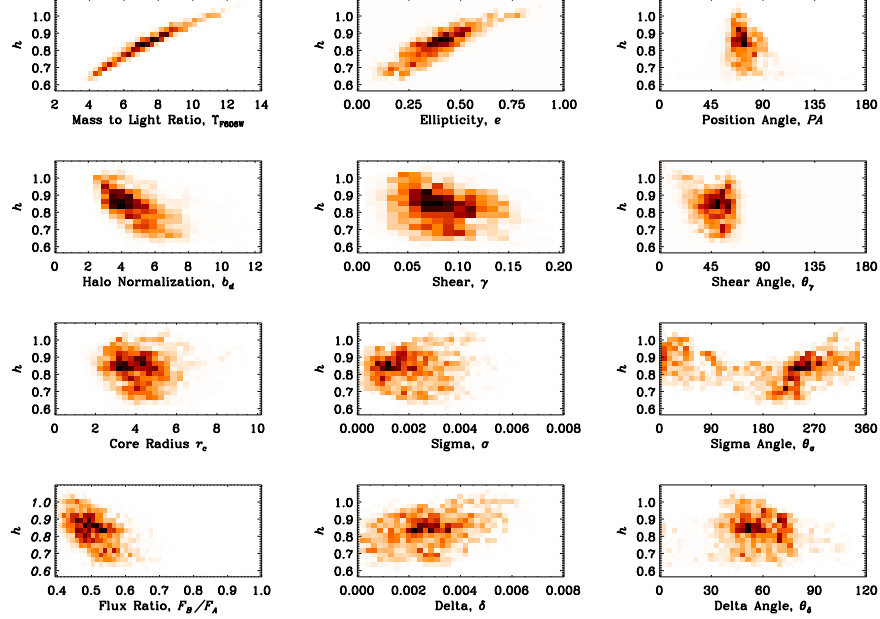


FIG. 5.— 2D histograms depicting the marginalized joint probability distributions $P(\theta, h)$ for each model parameter θ and the dimensionless Hubble constant h . (For an explanation of parameters, see Table 3.) We also show the model flux ratio in the lower left panel. The colorscale is linear in the probability density, running from black at the peak to white at zero. These results are based on dark matter models with a softened isothermal profile ($\alpha = 1$).

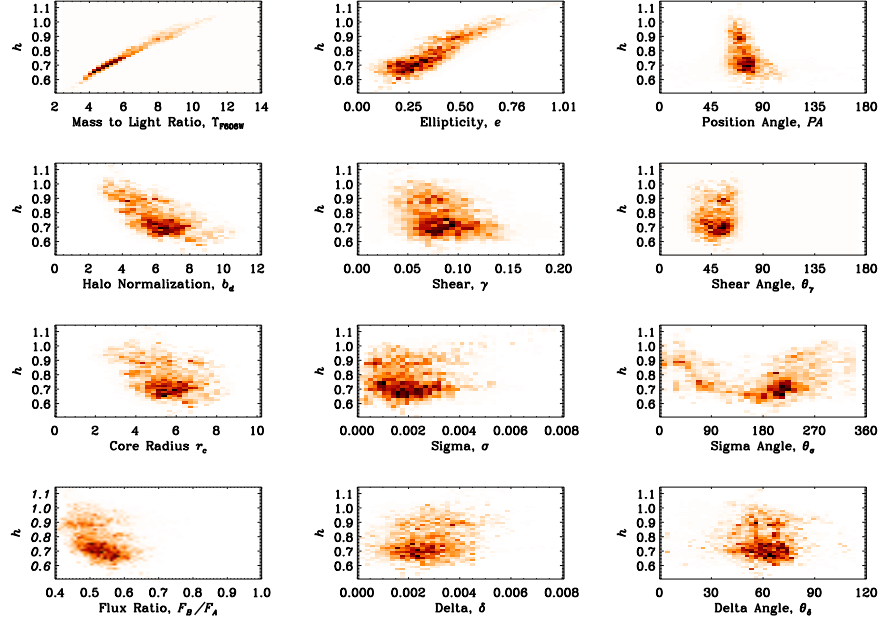


FIG. 6.— Similar to Fig. 5, but for models in which the dark matter halo has a power law profile that is steeper than isothermal ($\alpha = 0.5$).

to the degeneracy in Υ_{F606W} . Since the stellar component has a fixed angular structure whose position angle ($\sim 67^\circ$ – 82° , Fig. 3) does not quite match the necessary angular structure of the lens potential (with position angle closer to 63° , see Fig. 11), the dark matter component needs to make up the difference. The amount of compensation increases as the mass of the stellar component increases, so the halo ellipticity rises with Υ_{F606W} .

Figure 12 shows the corresponding caustics in the source plane. Generically, the tangential caustic is elongated along a roughly NE-SW direction and extends beyond the radial

caustic. There is some variation among the models, but the main effect is just an overall rescaling by $1 - \kappa_E$, where κ_E is the convergence at the Einstein radius (which is related to $\kappa_{s,30''}$). Many of our newly discovered sources are inferred to lie within the tangential caustic and should therefore have four images. Since we did not necessarily identify these as quad systems in our original detections (§2.3), it is interesting to examine the predicted counter-images. Figure 13 shows all the predicted images of the quadruply-imaged sources, for comparison with the detected images shown in Figure 4. (We show results for one particular model, but results for other

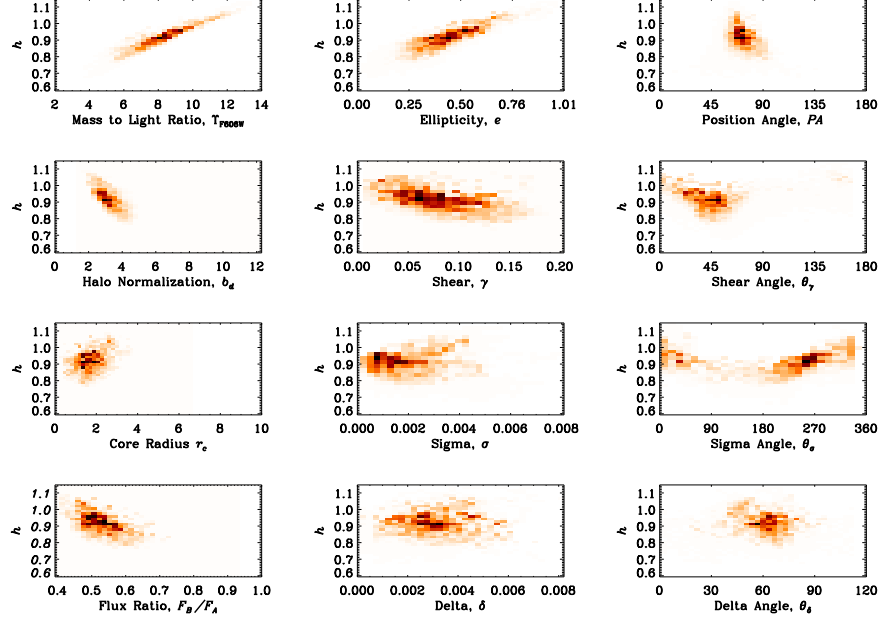


FIG. 7.— Similar to Fig. 5, but for models in which the dark matter halos has a power law profile that is shallower than isothermal ($\alpha = 1.5$).

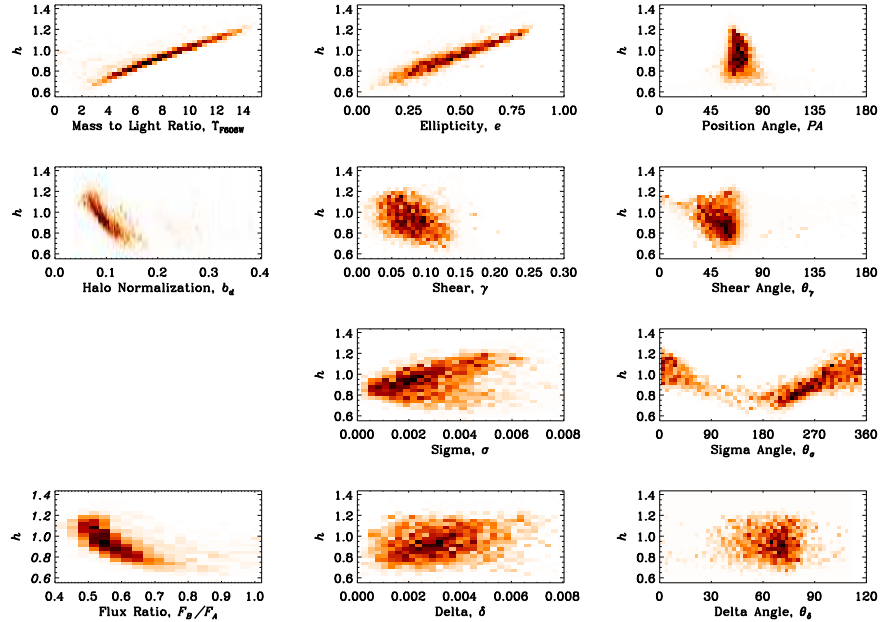


FIG. 8.— Similar to Fig. 5, but for models with an NFW dark matter halo. Here we do not show $P(r_s, h)$ since we discretely sample the scale radius (see §3.4).

models are similar.) We see that there are some predicted images that lie in relatively blank regions West of quasar B and South of quasar A. This is not a concern, however, because the undetected images have magnifications that are a factor of 10–100 smaller than the detected images lying to the East of quasar B, so their predicted fluxes lie well below the noise level of the HST image. Some of the predicted counter-images (among the ones indicated by diamonds) are not so far below the noise, but they still lack clear peak positions and thus cannot currently provide further robust constraints on lens models.

We consider one additional source of strong lensing con-

straints, namely extended images of the quasar host galaxy observed with HST/NICMOS by Keeton et al. (2000). Following Keeton et al., we analyze the arcs by taking the resolved arc around quasar A, mapping it pixel-by-pixel to the source plane using the lens model of interest, then mapping the reconstructed source back to the image plane to predict the arc around quasar B. Generally, we find that all models generated from our ACS data reproduce the NICMOS arcs comparably well; the NICMOS arcs do not restrict the range of models significantly better than the ACS data. We infer that the ACS data have captured most of the information present in the NICMOS arcs, which is not surprising given that the ACS

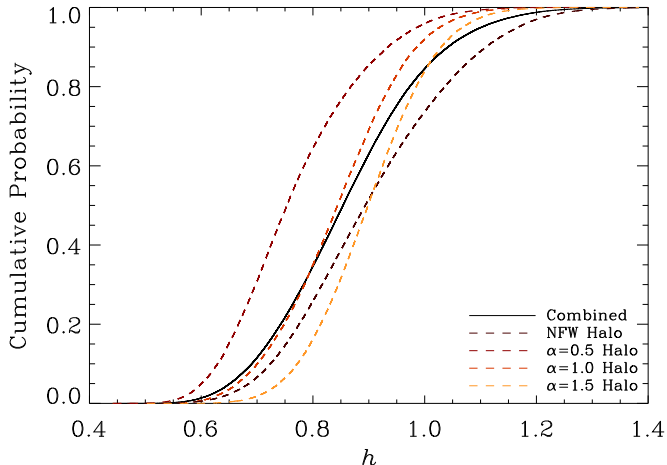


FIG. 9.— Cumulative posterior probability distribution for the dimensionless Hubble constant h for our four dark matter halo profiles. The solid black curve shows the result of combining these distributions, weighted by their relative probabilities.

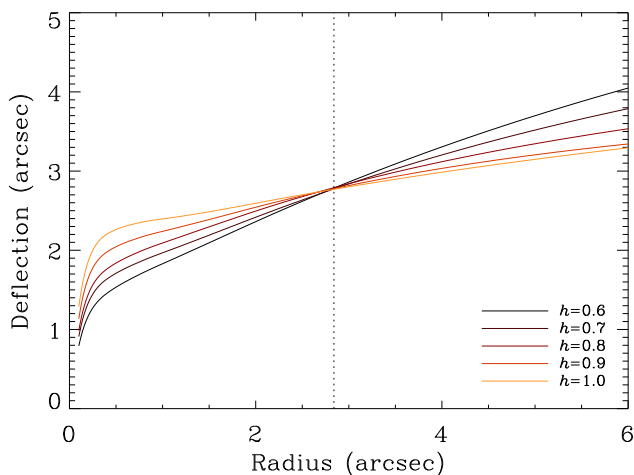


FIG. 10.— Monopole deflection profile for models with $h = 0.60, 0.70, 0.80, 0.90$ and 1.00 . We actually plot the mean profile for all models within ± 0.005 of the nominal h value; the scatter among such models is $< 2\%$ across all radii and does not depend systematically on the particular dark matter profile. The vertical dotted line indicates the Einstein radius at $R_{ein} = 2.84''$. The scatter among models drops to $< 0.5\%$ in the vicinity of R_{ein} , indicating a robust and tight constraint on the Einstein radius.

and NICMOS data span similar spatial regions and (presumably) both come from the lensed quasar host galaxy. Compared with the NICMOS arcs, the ACS data are somewhat cleaner to interpret because they avoid complicated interpolations to and from the image plane and offer a more straightforward counting of degrees of freedom. We take the compatibility of the NICMOS and ACS data as additional reassurance that the mapping of faint lensed features (§2.3) has been done correctly.

4.2. Quasar Flux Ratio

So far we have only considered image positions as lensing constraints. In order to include some information about the lensing magnification, we consider measurements of the quasar flux ratio. Bernstein & Fischer (1999) and Keeton et

al. (2000) used the delay corrected VLA measurements at 4 cm and 6 cm by Haarsma et al. (1999) to constrain the quasar core flux ratio. While the VLA cannot resolve out the relative contributions of radio components, if the jets are invariant on decadal time scales, the ratio of the radio *fluctuations* gives a measurement of the core flux ratio. With this assumption, Haarsma et al. derive the core flux ratio to be 0.74 ± 0.02 . Before applying this constraint to our lens models, we must consider whether our models should be expected to fit the observed flux ratio. The issue is whether dark matter substructure may perturb the flux ratio (e.g., Mao & Schneider 1998; Metcalf & Madau 2001; Dalal & Kochanek 2002; Chiba et al. 2005; MacLeod et al. 2009) in a way that our smooth models cannot reproduce.

High-resolution VLBI measurements show that the quasar images are $\lesssim 1.2$ mas in size (Gorenstein et al. 1988b), which corresponds to a size for the emission region in the source plane of $\lesssim 0.9$ mas or $\lesssim 5.4h^{-1}$ pc. We use the methods of Dobler & Keeton (2006) to estimate how a source of this size would be affected by an isothermal sphere clump placed near one of the images. We find that a clump of mass $\gtrsim 10^6 M_\odot$ can easily change the lensing magnification by a factor of order unity, and N -body simulations predict such subhalos to be abundant ($\gtrsim 10^3$) in a galaxy with a mass of $\sim 10^{13} M_\odot$ (e.g., Springel et al. 2005; Angulo et al. 2008). Apparently we should not discount the possibility that substructure plays a significant role in the observed VLA flux ratio.

Our basic models generally predict a flux ratio in the vicinity of ~ 0.5 with at most a tail extended to the range of the VLA measurement (see Figs. 5–8 and Table 5). The discrepancy could be interpreted as evidence that the VLA flux ratio is indeed perturbed by substructure. Further support for this hypothesis comes from the fact that the magnification ratio inferred from the resolved radio jets is different from the ratio for the quasar cores, and closer to the smooth model prediction (Bonometti 1985; Gorenstein et al. 1988b; Conner et al. 1992). We should be careful, of course, not to think that a measurement that disagrees with our smooth models is “wrong” and one that agrees is “right” — or to assume that any discrepancy involving a flux ratio automatically implies dark matter substructure. Nevertheless, we conclude that existing evidence shows the flux ratio to be very intriguing and worthy of further study, both on its own and as possible evidence for substructure in Q0957.

With this in mind, it is not clear how strongly we should impose the VLA flux ratio as a constraint on our models. We consider using the measurement but inflating the errorbar by various factors to obtain a range of constraints from strong to weak. Figure 14 shows the marginalized cumulative posterior probability distribution for h for the different cases. The flux ratio constraint tends to reduce the median value of h and tighten the distribution. While such a result seems enticing, we caution that it may be artificial if the flux ratio is really perturbed by substructure which is absent from our model. Given the concerns, we choose not to use the flux ratio as a constraint for our final results. If there were some way to determine the “macro” flux ratio, however, that might help improve constraints on h .

4.3. Stellar Mass to Light Ratio

As shown in Figures 5–8, our models demonstrate a strong correlation between h and Υ_{F606W} , the stellar mass-to-light ratio, as a consequence of the radial profile degeneracy in lens-

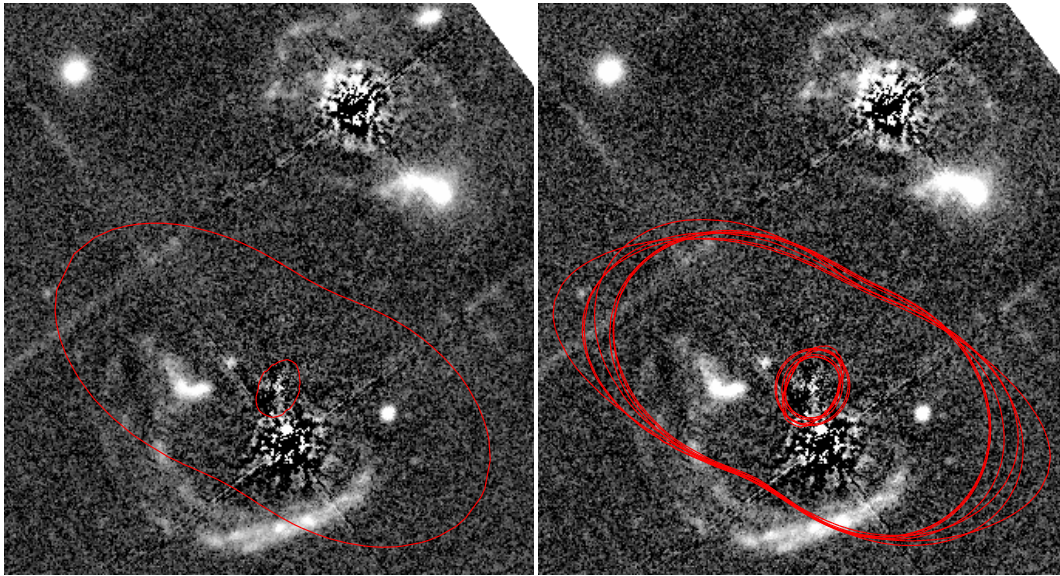


FIG. 11.— (a, left) A typical critical curve resulting from the new image constraints in Table 2. Notice the fold image pairs that the curve runs through South and East of quasar B. (b, right) Critical curves corresponding to models with minimal/maximal values of different parameters, for our models with an NFW dark matter halo (results are similar for other model classes). The critical curves show little variation along the semi-minor axis due to strong constraints from new images. Significant variation still exists along the semi-major axis of the curves.

ing. Any external constraints on Υ_{F606W} could not only narrow the overall parameter space but also tighten constraints on h . It is possible to obtain such constraints from stellar population synthesis (SPS) models thanks to the fact that we have excellent HST photometry of a relatively “simple,” old stellar population in the lens galaxy.

We use two sets of SPS models. The first are the Flexible Stellar Population Synthesis (FSPS) models of Conroy et al. (2009). These models exhibit enormous flexibility and are aimed at addressing many of the uncertainties of SPS models. In particular, the user can not only consider the traditional effects of varying the star formation history, star formation epoch, metallicity, initial mass function (IMF), and dust, but also account for various treatments of the thermally pulsating asymptotic giant branch (TP-AGB), blue stragglers, and blue horizontal branch stars. See Conroy et al. (2009) for details of the FSPS models and the SPS uncertainties they address. Using the FSPS models, we follow the treatment of Conroy et al., adjusting 9 models parameters (see Table 4) that include the effects of varying the epoch of star formation, the star formation history, and dust. We consider six metallicities from 50% to 160% Solar using a Chabrier IMF (Chabrier 2003).

The second set of SPS models we use are from Maraston et al. (2009). These models are based on the same simple stellar populations (SSPs) as Maraston (2005), which treat the TP-AGB contribution to the SEDs, but also include a metal poor ($[Z/H] = -2.2$) population comprising 3% of the mass. As shown by Maraston et al. (2009), these models provide a good fit to the optical colors of galaxies in the Luminous Red Galaxy (LRG) sample from the Sloan Digital Sky Survey. This is encouraging because SPS models have historically had trouble fitting LRG colors (e.g., Eisenstein et al. 2001; Wake et al. 2006). Since the lens galaxy in Q0957 is luminous ($L \sim 6.5L_*$) and red ($m_{F606W} - m_{F814W} = 1.057$), we postulate that these models should provide a good fit the galaxy’s spectral energy distribution. To account for variation of the lens galaxy from the SSPs of Maraston et al., we allow for variation in the redshift at which star formation begins, the star formation history, and dust. As in our FSPS models, we

allow star formation to begin anywhere from the CMB redshift, $z = 1089$, to the redshift of the lens, $z = 0.361$. We adopt the star formation rate

$$\Psi(t) = \frac{1-C}{\tau} \frac{e^{-t/\tau}}{e^{-T(z_{form})/\tau} - e^{-T(z_l)/\tau}} + \frac{C}{T(z_l) - T(z_{form})}, \quad T(z_{form}) \leq t \leq T(z_l), \quad (25)$$

where C is the fraction of stars formed at a constant rate, τ is the e-folding time of the star formation rate, and $T(z)$ denotes the age of the universe at redshift z . This form of the star formation rate has the advantage of smoothly varying from a SSP to a constant star formation history. For dust, we consider the two-parameter model of Charlot & Fall (2000) which includes the effect of dust around young stars as well as a diffuse dust component. Parameters for our Maraston SPS models are summarized in Table 4.

As constraints on the SPS models, we use our measurements of the F606W and F814W magnitudes of the lens galaxy (see Table 1) together with a reanalysis of the NICMOS/F160W image obtained by Keeton et al. (2000). The revised AB magnitude $m_{F160W,AB} = 16.84 \pm 0.15$ (Chien Peng, private communication) differs somewhat from the originally reported value because it is based on a more sophisticated deconvolution of the lens galaxy from the quasar images and host arcs. We correct for Galactic extinction using the methods of Schlegel et al. (1998), finding the value of $E(B-V) = 0.0095$.

Initial modeling found that large values of dust extinction, extending to $A_{F606W} > 2.0$ mag, were allowed in the SPS models. This was unexpected since early type galaxies are known to have modest dust content (e.g., Schawinski et al. 2007). In lensed systems, differential extinction measurements have shown that lenses typically exhibit smaller values of dust extinction than found in nearby, late-type galaxies: Elíasdóttir et al. (2006) find a mean extinction of $A_V = 0.56 \pm 0.04$ in a sample of 10 lenses (also see Falco et al. 1999). For Q0957 we could in principle rely on previous attempts to measure

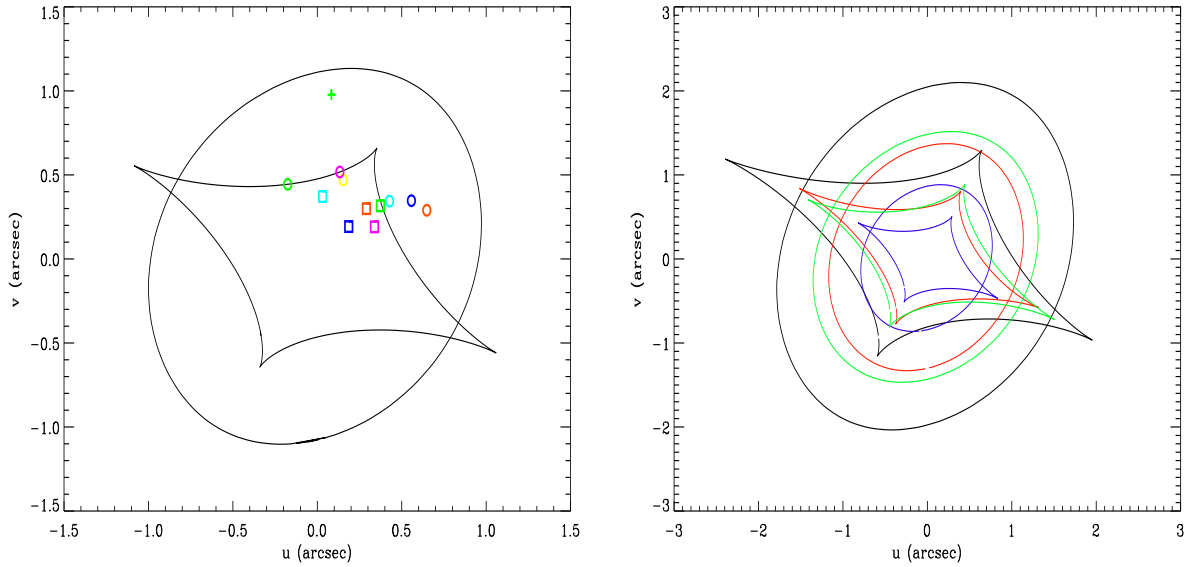


FIG. 12.— (a, left) Source plane caustic corresponding to the critical curve shown in Fig. 11a. The points show the positions of the sources corresponding to the observed images, with the same shape and color scheme as in Fig. 4. (b, right) Source plane caustics corresponding to the critical curves shown in Fig. 11b. The main variation is an overall rescaling due to different values of the convergence in the vicinity of the Einstein radius.

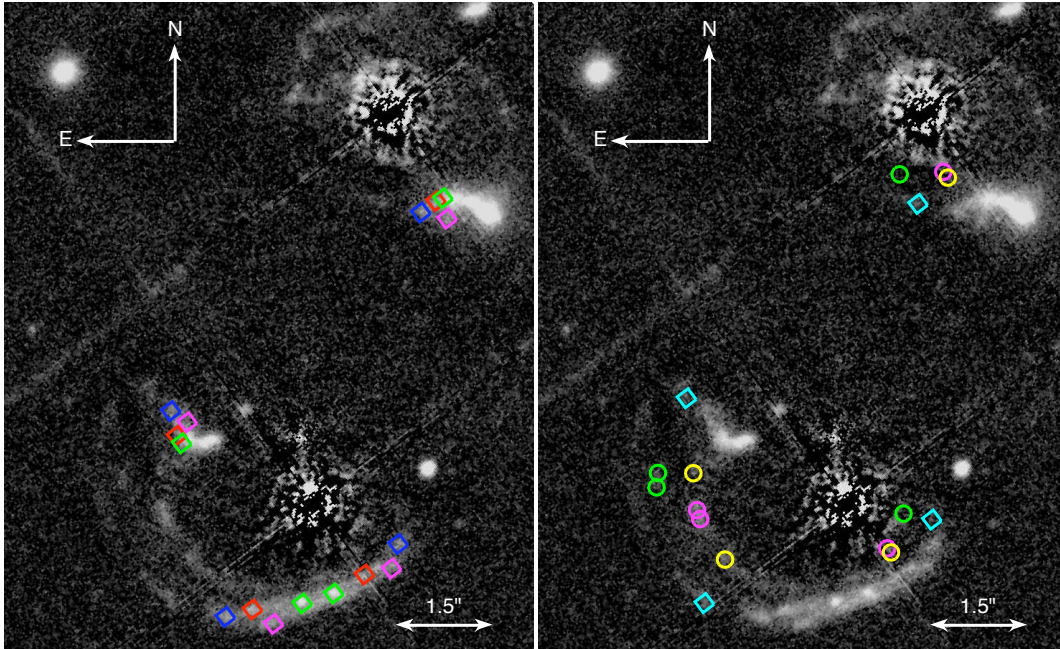


FIG. 13.— Predicted images of all sources that lie inside the tangential caustic for our lens models. Results are shown for the same model as Figure 12a but are similar for other models. The two panels correspond to different sets of sources, with the same arrangement as Figure 4. There are some predicted images shown here that have not been detected (i.e., they do not appear in Fig. 4); they are predicted to be below the noise in our HST data.

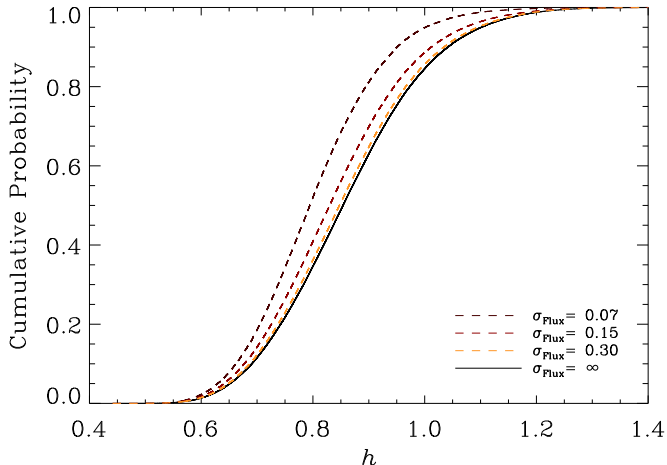


FIG. 14.— Cumulative posterior probability distribution for the dimensionless Hubble constant h with different assumptions about the constraint from the quasar radio flux ratio. The solid black line shows our fiducial results using the image positions alone (from Fig. 9). The dashed lines show how the results change when we impose constraints from the VLA flux ratio constraints (Haarsma et al. 1999) with the uncertainties increased by a factor of 3.5, 7.5, and 15, representing different levels at which effects from substructure might be understood. These values are consistent with an increase in the magnification of image B by a factor of 1.35, 1.20, and 1.0 due to a subhalo of mass $\gtrsim 10^6 M_\odot$. While adding flux constraints clearly tightens the h distribution, we do not include them in our final h distribution since we do not currently understand the extent to which substructure may be important in Q0957.

the dust content of the lens galaxy, but the results are puzzling. Goicoechea et al. (2005) used HST/STIS observations to measure the flux ratio $F_B/F_A > 1$ at optical and ultraviolet wavelengths (also see the delay corrected ratios of Colley et al. 2003), which stands in stark contrast to the VLA measurement $F_B/F_A = 0.74 \pm 0.02$ and our models predictions. To explain this difference Goicoechea et al. invoke dust clouds in front of image A leading to extinction $A_V = 0.30$. It is counterintuitive to think that image A (at $18.6 h^{-1}$ kpc from the center of the galaxy) is more heavily extinguished than image B (just $3.7 h^{-1}$ kpc from the center). If extinction is indeed the cause of the wavelength dependence in the flux ratios, it remains unclear how the dust is distributed throughout the rest of the galaxy, whether it is clumpy and extends to large radii in other directions. For all these reasons, we choose not to constrain the dust in the SPS models to a particular value. Nevertheless, in order to avoid unreasonable large extinction values we impose a weak, exponential prior of the form $e^{-A_{F606W}/1.0 \text{ mag}}$.

In order to derive constraints on Υ_{F606W} , we set up an MCMC analysis similar to what we use for lens models (see §3.4) to sample the posterior probability distribution. Since the value of Υ_{F606W} depends on h (principally through the age of the universe as a function of redshift), we run the MCMC analysis for discrete values of h from 0.50 to 1.45 in steps of $\Delta h = 0.025$; the small steps ensure that the median and range of Υ_{F606W} do not vary by more than 3% from one h value to the next, so we can interpolate accurately. Figure 15 shows the cumulative distributions for Υ_{F606W} for different values of h , from both FSPS and Maraston models. In general, both models fit the observed F606W–F814W and F606W–F160W colors well ($\chi^2_{\text{reduced}} \leq 1$), but the FSPS models yield a larger range for Υ_{F606W} . This is not surprising given the amount of freedom available in the FSPS models. Previous studies of

massive ellipticals found values of Υ_B of $\sim 4-10$ (e.g., Gerhard et al. 2001; Grillo et al. 2009), in good agreement with the values found here.⁹

Figure 16 shows what happens to the posterior probability distribution for the Hubble constant when we impose the SPS constraints on Υ_{F606W} . Using the FSPS models has little effect on the h distribution, because these models allow for a large range of values for Υ_{F606W} . The Maraston models, by contrast, favor $\Upsilon_{F606W} \sim 4.5-6.5$ and such values tend to reduce the median h and tighten the distribution. Clearly it is important to understand why the FSPS and Maraston models differ as to whether high values of Υ_{F606W} are acceptable. Figure 17 shows that the high Υ_{F606W} values attained in FSPS models correspond to large values of extinction — values that seem surprising for a luminous early-type galaxy in a modest cluster at redshift $z = 0.361$. We infer that the flexibility of FSPS models is allowing them to reproduce the observed colors of the galaxy even with models that do not make much sense astrophysically. One way to reconcile the FSPS and Maraston models is to constrain the amount of dust in our FSPS models. We find that adopting an extinction prior of $A_{F606W} = 0.45 \pm 0.2$ would bring the FSPS constraints on Υ_{F606W} into agreement with those from the Maraston models. Imposing such a prior has little effect on the Υ_{F606W} constraints from the Maraston models since those models show little or no correlation between dust extinction and Υ_{F606W} .

Ultimately we need to decide what to use for our final constraints on Υ_{F606W} . Since the Maraston models are constructed to match the SDSS LRG sample and require no ad hoc assumptions about the dust content of the lens galaxy, we elect to use them when reporting our final determination of h and model parameters (see Table 6). With these constraints on Υ_{F606W} we find $H_0 = 79.3^{+6.7}_{-8.5} \text{ km s}^{-1} \text{ Mpc}^{-1}$ (68% CL).

4.4. Physical Properties of NFW Halos

When fitting models with an NFW dark matter halo, we previously took both r_s and $\kappa_s = \rho_s r_s / \Sigma_{\text{crit}}$ to be free parameters. However, in N -body simulations the two NFW parameters are actually related to one another, albeit with some scatter. We now consider whether our lens model parameters have reasonable values in general, and whether they are consistent with the correlation found in simulated halos.

Parameterizing NFW halos with the virial mass M_{vir} and concentration c_v , Macciò et al. (2007) find that the parameters are related by $c_v(z) = 213^{+40}_{-34} M_{\text{vir}}^{-0.109 \pm 0.005} (1+z)^{-1}$. We can express our lens model parameters in terms of M_{vir} and c_v as follows:

$$\kappa_s = \left(\frac{1+z}{c} \right)^2 \left[\frac{1}{2} (GM_{\text{vir}})^{1/2} H_0^2 \Omega_m \Delta_{\text{vir}} \right]^{2/3} \quad (26)$$

$$\times \frac{D_{ol} D_{ls}}{D_{os}} c_v^2 \left[\ln(1+c_v) - \frac{c_v}{1+c_v} \right]^{-1}$$

$$r_s = \frac{1}{c_v(1+z)} \left[\frac{2GM_{\text{vir}}}{H_0^2 \Omega_m \Delta_{\text{vir}}} \right]^{1/3} \quad (27)$$

where $\Delta_{\text{vir}} = 98$ is the virial overdensity (Mainini et al. 2003; Macciò et al. 2007). Figure 18 compares our recovered model values of r_s and κ_s with expectations based on the Macciò et al. (2007) relation for different values of the NFW halo mass. The first point is that the model parameters do indeed have

⁹ At a redshift of $z = 0.36$, observed Υ_{F606W} corresponds to rest frame Υ_B .

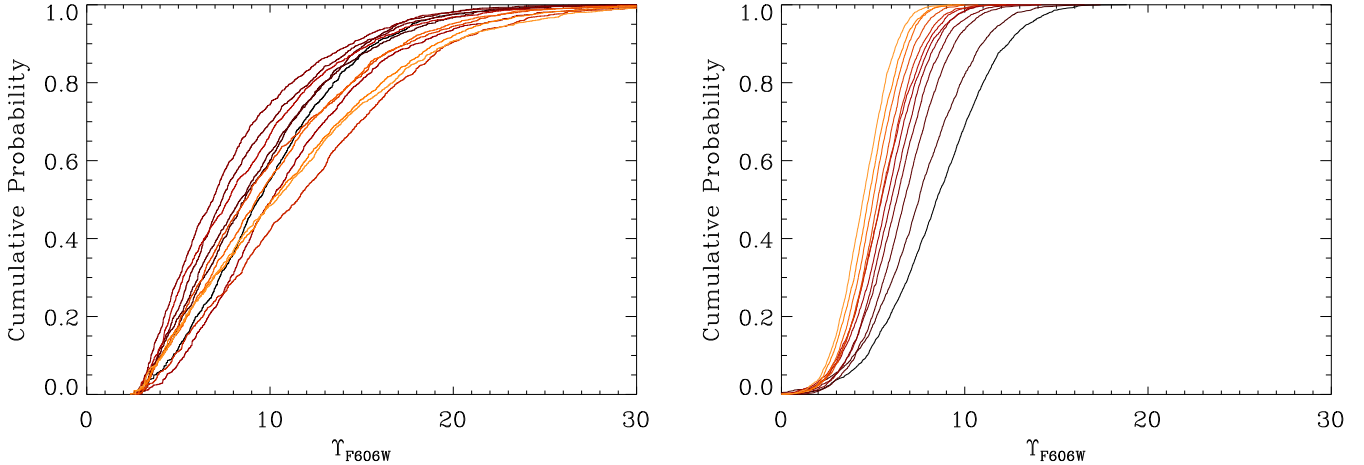


FIG. 15.— Cumulative posterior probability distributions for the stellar mass to light ratio, Υ_{F606W} . The different curves correspond to different values of h , varying from 0.55 (black) to 1.10 (light orange) in increments of 0.05. (a, left) Results from the FSPS models of Conroy et al. (2009). (b, right) Results from the SPS models of Maraston et al. (2009). The FSPS models tend to produce higher values of Υ_{F606W} with more scatter than the Maraston models. Also, the FSPS models are not as *systematically* dependent on h , presumably because the large freedom in the models dominates the distribution of Υ_{F606W} .

reasonable values. Going into more detail, we see that our models with small scale radii ($r_s < 10''$) are consistent with relatively low cluster masses ($M_{vir} \lesssim 10^{13.5} M_\odot$) but concentrations that are 3–6 σ above the median for that mass. As the scale radius increases, our models follow a track corresponding to increasing mass and decreasing concentration; indeed, lens models with $r_s \gtrsim 200''$ require an extraordinarily large mass of $M_{vir} \gtrsim 10^{15} M_\odot$. Such a large mass seems unreasonable for a fairly modest galaxy cluster, especially considering that X-ray measurements imply a mass within $1 h_{75}^{-1}$ Mpc of $9.9_{-3.8}^{+1.9} \times 10^{13} M_\odot$ (Chartas et al. 2002). Therefore, we argue that our models with $r_s \gtrsim 200''$ are disfavored but models with $r_s \lesssim 200''$ have parameters that seem reasonable in comparison with simulated NFW halos. We note that recovering a concentration that is a few sigma above the median is not necessarily a concern, because there may be a selection bias such that a high concentration increases the lensing cross section

(see, e.g., Mandelbaum et al. 2009).

5. DISCUSSION AND CONCLUSIONS

Since its discovery in 1979, Q0957 has presented many puzzles that we still cannot definitively solve. Nevertheless, by combining new HST/ACS data and stellar population synthesis models, we have presented a consistent picture of lensing in this system using a realistic treatment of both the stellar and dark matter components of the mass distribution. In §5.1 we discuss our results regarding measurements of H_0 with Q0957. Turning the tables, in §5.2 we adopt priors on H_0 from other measurements and examine the inferred properties of the lens mass distribution. Looking ahead, in §5.3 we discuss potential ways in which these measurements can be improved.

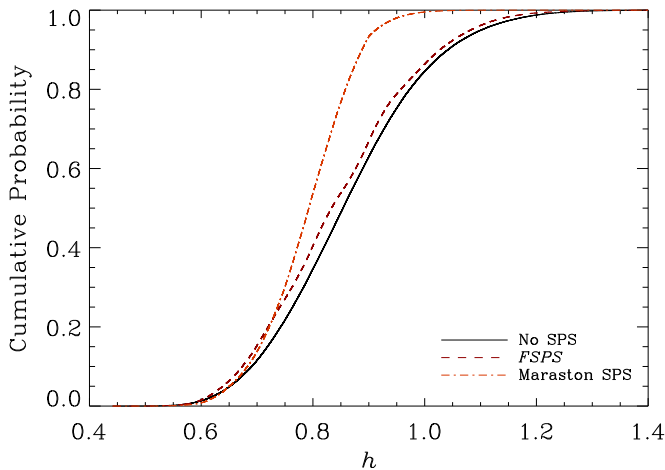


FIG. 16.— Cumulative posterior probability distribution for h with and without constraints from SPS models. Since the Maraston SPS models have been shown to fit LRG colors from the SDSS, we adopt them when quoting final values of h and model parameters. We find $H_0 = 79.3_{-8.5}^{+6.7}$ km s $^{-1}$ Mpc $^{-1}$ (68% CL).

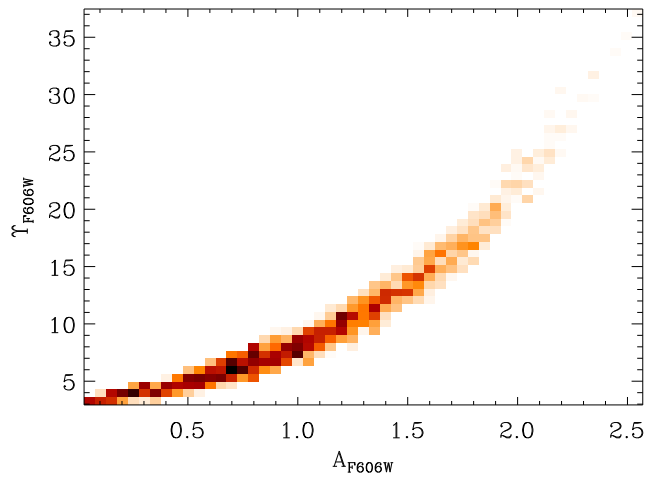


FIG. 17.— 2D histogram showing the joint probability distribution for the stellar mass-to-light ratio, Υ_{F606W} , and the amount of extinction in the F606W band, from FSPS models. As the amount of extinction increases, the model magnitude in the F606W filter increases, leading to a larger values of Υ_{F606W} . Results are shown for models with $h = 0.7$ and Solar metallicity, but the distributions for other values of h and metallicity exhibit a similar behavior.

5.1. Hubble Constant

Motivated by our new ACS data, we conducted a joint strong+weak lensing analysis in the hope of obtaining the best constraints to date from Q0957. In §4.1 we found $H_0 = 85_{-13}^{+14}$ km s⁻¹ Mpc⁻¹ (68% CL) on the basis of lensing alone. This result is higher than, but still consistent with, measurements from other recent lensing (e.g., Jakobsson et al. 2005; Paraficz et al. 2009; Oguri 2007) and non-lensing (e.g., Freedman et al. 2001; Riess et al. 2009; Dunkley et al. 2008; Komatsu et al. 2008) studies. In spite of the extensive lensing data we have obtained, the uncertainty in H_0 from Q0957 is still larger than from most other lenses (see Fig. 1).

One source of uncertainty in Q0957 is the sheer complexity of the potential: with ellipticity, shear, and higher-order environmental terms to play with, models can find a wide range of combinations that fit the data well (see Figs. 5–8). The main systematic effect in lens models is a correlation between h and the stellar mass-to-light ratio of the lens galaxy. Varying Υ_{F606W} changes the balance between stars and dark matter in the lens galaxy, which modifies the net density profile, which then affects h through the radial profile degeneracy (e.g., Kochanek 2002). We can actually turn this degeneracy to our advantage if we can place independent constraints on the stellar mass-to-light ratio. In §4.3 we used the stellar population synthesis models from Maraston et al. (2009) to constrain Υ_{F606W} and thereby reduce the uncertainties in our Hubble constant determination to $H_0 = 79.3_{-8.5}^{+6.7}$ km s⁻¹ Mpc⁻¹ (68% CL).

While this is a significant reduction in the uncertainty for H_0 from Q0957, we caution that SPS models are still improving and may ultimately be even more complicated than the Maraston models. When we used the FSPS models of Conroy et al. (2009), for example, we did not see much tightening of the H_0 constraints relative to lensing alone; and we traced the trouble to uncertainties in the amount of dust extinction in

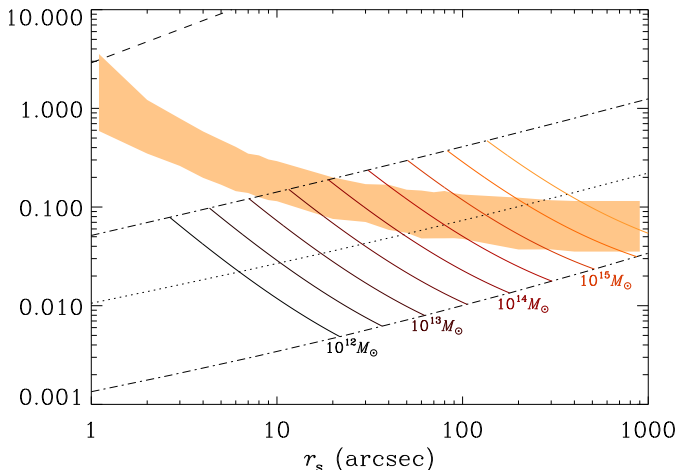


FIG. 18.— The space of scale radius, r_s , and halo normalization, κ_s , for NFW halos at the lens redshift $z = 0.361$. The shaded region indicates the parameter range occupied by our lens models with an NFW dark matter halo. The dotted curve shows the expected relation between κ_s and r_s based on the median concentration/mass relation found in N -body simulations by Maccio et al. (2007), while the dot-dash curves show the $\pm 3\sigma$ range, and the dashed curve in the upper left corner lies 6σ above the median. The colored solid curves represent the theoretical predictions at fixed virial mass, with the concentration varying $\pm 3\sigma$ around the median, ranging from $10^{12} M_\odot$ (black) to $10^{16} M_\odot$ (orange) in steps of 0.5 dex.

the lens galaxy. There is one additional source of uncertainty in SPS models that we did not explicitly address, namely the IMF. Variations in the IMF can alter the colors and mass-to-light ratios of SPS models (e.g., Conroy et al. 2009). In particular, a more bottom-heavy IMF (e.g., Salpeter) would raise the inferred value of the Υ_{F606W} and hence our median value of H_0 , while a more top-heavy IMF would have the opposite effect. For the Maraston SPS models, variations in the IMF must be relatively small or the models would cease to provide a good fit to the SDSS LRG sample. We attempt to compensate for IMF-related variations by allowing broad ranges for the star formation history, star formation epoch, and dust. Nevertheless, this remains an unknown, but presumably small, uncertainty in our models. Clearly there is a lot of room for improvement with a better understanding of the stellar population of the lens galaxy (see §5.3).

5.2. Mass Distribution

Instead of trying to measure H_0 ourselves, we can choose to place external priors on H_0 to see how well we can understand the mass distribution of the lens. We consider two determinations of H_0 : the refurbished distance ladder measurement of $H_0 = 74.2 \pm 3.6$ km s⁻¹ Mpc⁻¹ by Riess et al. (2009), and the combined WMAP5+SNe+BAO value of $H_0 = 70.5 \pm 1.3$ from Komatsu et al. (2008). In Table 7 we show the model parameters recovered from this approach.

Examining the relative probabilities of the models, it is clear that the lensing data favor a power law profile of index $\alpha = 0.5$ or 1.0 over $\alpha = 1.5$ or an NFW profile. Both of the favored models exhibit relatively large core radii: $a = 5.8_{-1.0}^{+1.1}$ arcsec for $\alpha = 0.5$, or $a = 4.2_{-0.7}^{+1.0}$ arcsec for $\alpha = 1$. Given the reduced probability of our NFW models, we conclude that lensing provides strong evidence for a constant-density core (rather than a cusp) in the dark matter halo of Q0957.

In Figure 10 we showed that Q0957 exhibits a rising deflection profile, analogous to a rising rotation curve and indicative of a net density profile shallower than isothermal. While this is not the first case of a lens with a rising rotation curve (see Kochanek et al. 2006), the origin of phenomenon is unclear. One possible explanation involves the special location of the lens galaxy. As the central galaxy in a modest cluster, the lens is embedded in the most concentrated part of a massive dark matter halo. The higher than average surface density of dark matter leads to a shallow density profile and a rising deflection curve. To further explore this idea, we shown in Figure 19 the fraction of the deflection contributed by dark matter as a function of radius. This is equivalent to the projected enclosed dark matter fraction as a function of radius. At the effective radius, dark matter constitutes $(50 \pm 7)\%$ or $(57 \pm 7)\%$ of the enclosed mass (assuming the Riess or Komatsu priors on H_0 , respectively). Such values are well above the minimum dark matter fraction found $(38 \pm 7)\%$ for galaxies in the SLACS survey (Bolton et al. 2008), and are greater than 16 of the 22 lens systems considered by (Jiang & Kochanek 2007). It is not very surprising, of course, to find a relatively large dark matter fraction in a brightest cluster galaxy.

We find the the dark matter halo in Q0957 must be well aligned with stellar mass distribution. With either the Riess or Komatsu H_0 priors, we find the position angle of the dark matter halo to be $\theta_e = 73_{-10}^{+9}$ deg, in good agreement with the measured position angle of the stellar component $\theta_* = 71 \pm 5$ deg at large radii ($> 5''$). Perhaps more interesting is that the ellipticity of the dark matter appears to be in good agreement

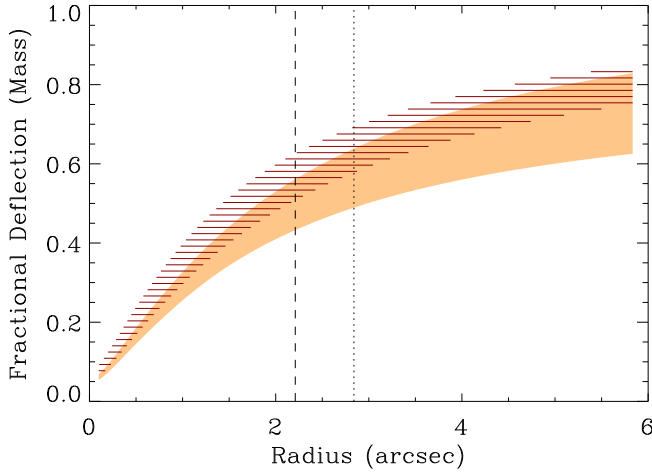


FIG. 19.— Fraction of the monopole deflection contributed by the dark matter halo, as a function of radius. Since $\alpha(r) \propto M(r)/r$, this plot also depicts the enclosed projected dark matter fraction as a function of radius. The vertical dotted line indicates the Einstein radius at $R_{\text{ein}} = 2.84''$ while the vertical dashed line marks the effective radius of the stellar light profile at $R_e = 2.21''$. The shaded regions show results from our models when we adopt different priors on the Hubble constant: the orange region corresponds to assuming $H_0 = 74.2 \pm 3.6 \text{ km s}^{-1} \text{ Mpc}^{-1}$ from Riess et al. (2009), while the region indicated with red horizontal lines corresponds to $H_0 = 70.5 \pm 1.3 \text{ km s}^{-1} \text{ Mpc}^{-1}$ from Komatsu et al. (2008).

with that of the stellar distribution. We find the ellipticity of the dark matter to be $e = 0.28^{+0.06}_{-0.07}$ or $e = 0.25^{+0.07}_{-0.09}$ for the Riess or Komatsu H_0 values, in good agreement with the measured value of the stellar ellipticity $e_* \sim 0.3$ at large radii.

In general, we find that improving H_0 constraints from 5% to 2% has little impact on our understanding of the mass distribution, because most of our model parameters have little or no correlation with H_0 . The only significant exception is in our determination of the stellar mass to light ratio, Υ_{F606W} . We find $\Upsilon_{\text{F606W}} = 5.5^{+0.9}_{-0.5}$ using the Riess value for H_0 , versus $\Upsilon_{\text{F606W}} = 5.5^{+0.2}_{-0.3}$ using the Komatsu value. For comparison, the Maraston SPS models give $\Upsilon_{\text{F606W}} = 5.9 \pm 1.9$. It is interesting to see that combining lensing with H_0 priors can provide excellent constraints on stellar populations, which may prove useful as SPS laboratories as multi-wavelength datasets for well-studied lenses grow.

We found the intriguing result that our models favor a quasar flux ratio around $F_B/F_A = 0.53 \pm 0.06$, which is substantially different from the radio measurement of $F_B/F_A = 0.74 \pm 0.02$. Since the radio emission is free from extinction by dust, and should be insensitive to microlensing by stars, we infer the quasar flux ratio in Q0957 seems to be “anomalous.” The putative anomaly presumably indicates additional complexity in the lens potential. While the nature of that complexity is not yet clear, it is worth noting that dark matter substructure can easily produce flux ratio anomalies (e.g., Mao & Schneider 1998; Metcalf & Madau 2001; Dalal & Kochanek 2002; Chiba et al. 2005; MacLeod et al. 2009). Invoking substructure as an explanation seems especially enticing because the radio jets, a mere 80 mas away from the quasar images, have a flux ratio of 0.61 ± 0.04 (Bonometti 1985), in much better agreement with the macro models. While we cannot definitively identify substructure from the present analysis, the evidence is fascinating and warrants future study.

5.3. Future Prospects

Looking ahead, there are several ways in which we can hope to improve the measurement of H_0 in Q0957. Following this work, the best improvements are likely to come from a better understanding of the stellar population and Υ_{F606W} . In the near term, an extension of the photometric data to both bluer and redder wavelengths could reduce the uncertainties in existing SPS models and, therefore, the uncertainties in H_0 . Over the longer term, extensive photometry spanning UV/optical/infrared wavelengths, coupled with a better understanding of SPS uncertainties (e.g., TP-AGB stars, blue stragglers, IMF), should boost the reliability and reduce the uncertainties in the SPS technique.

Improved lensing constraints may also help. One source of systematic uncertainty in our models is the uncertainty in the measurement of the total convergence from weak lensing. Currently, the total convergence is measured to $\sim 34\%$ precision. Deeper imaging would be observationally expensive but worthwhile, especially if coupled with improved understanding of the point spread function and source redshift distribution for the weak lensing analysis. For strong lensing, we have noted that there are additional faint lensed features that we have not used, but that might further constrain the lensing critical curve (see the discussion accompanying Figs. 11 and 13). We note for the record that using the precise position and flux ratio constraints for the quasars is not likely to help us understand the (large-scale) mass distribution or H_0 any better; those data will ultimately be most useful for probing small-scale structure in the lens.

Finally, it is interesting to consider whether stellar dynamics data could further constrain our models. Previous studies have shown that joint lensing+dynamics analyses can provide more information than lensing alone about the mass distribution (e.g., Treu et al. 2006; Barnabè & Koopmans 2007). The joint approach has been used to good effect by the SLACS team to improve constraints on quantities like the total mass to light ratio and the slope of the inner density profile (Koopmans et al. 2006). For Q0957, Romanowsky & Kochanek (1999) have successfully combined information from stellar dynamics and lensing to tighten constraints on mass models. Adopting the measured central velocity dispersion from Tonry & Franx (1997), Romanowsky & Kochanek use orbit modeling techniques to constrain a spherical power law profile, measuring $H_0 = 61^{+13}_{-15} \text{ km s}^{-1} \text{ Mpc}^{-1}$ (2σ). While it is clear such an analysis would be useful to further constrain our models, it would require orbit modeling for each of our model classes, which is beyond the scope of this work. Furthermore, it would require a deprojection of the stellar component that we include in our models, which could be challenging (because of the varying ellipticity and orientation; cf. Figure 3) and would have uncertainties of its own.

We thank Claudia Maraston and Charlie Conroy for providing their SPS models as well as technical comments and assistance, Chien Peng for revised NICMOS photometry and helpful discussions, Andrew Baker and Chuck Joseph for helpful comments and suggestions, and Viviana Acquaviva for timely help and advice. We also thank the anonymous referee for constructive criticism. This work has been supported by grant HST-GO-10569 from the Space Telescope Science Institute, which is operated by the Association of Universities for Research in Astronomy, Inc., under NASA contract NAS5-26555. Additional support has come from the National

Science Foundation via grants AST-0747311 (RF and CRK)

and AST-0607667 (RN and GMB).

REFERENCES

- Anderson, J. & King, I. R., 2002, Instrument Science Report ACS 2006-01, <http://www.stsci.edu/hst/acs/documents/isrs/isr0601.ps>
- Angulo, R. E., Lacey, C. G., Baugh, C. M., & Frenk, C. S., 2009, MNRAS, 399, 983
- Auger, M. W., Fassnacht, C. D., Abrahamse, A. L., Lubin, L. M., & Squires, G. K., 2007, AJ, 134, 668
- Barkana, R., Lehár, J., Falco, E. E., Grogin, N. A., Keeton, C. R., & Shapiro, I. I., 1999, ApJ, 520, 479
- Barnabè, M. & Koopmans, L. V. E., 2007, ApJ, 666, 726
- Bartelmann, M., 1996, A&A, 313, 697
- Bernstein, G., Fischer, P., Tyson, J. A., & Rhee, G., 1997, ApJ, 483, 79
- Bernstein, G. & Fischer, P., 1999, ApJ, 118, 14
- Blandford, R. D., & Narayan, R., 1986, ApJ, 310, 568
- Dark Matter in the Universe, Proceedings of the 4th Jerusalem Winter School for Theoretical Physics, Jerusalem. World Scientific Publication, Singapore, 1987, p.133
- Bolton, A. S., Treu, T., Koopmans, L. V. E., Gavazzi, R., Moustakas, L. A., Burles, S., Schlegel, D. J., & Wayth, R., 2008, ApJ, 684, 248
- Bonometti, R. J., 1985, Ph.D. thesis, Massachusetts Institute of Technology
- Burud, I., Hjorth, J., Jaunsen, A. O., Anderson, M. I., Korhonen, H., Clasen, J. W., Pelt, J., Pijpers, F. P., Magain, P., & Østensen, 2000, ApJ, 544, 117
- Burud, I., Hjorth, J., Courbin, F., Cohen, J. G., Magain, P., Jaunsen, A. O., Kaas, A. A., Faure, C., & Letawe, G., 2002, A&A, 391, 481
- Burud, I., Courbin, F., Magain, P., Lidman, C., Hutseméckers, D., Kneib, J. P., Hjorth, J., Brewer, J., Pompei, E., Germany, L., Pritchard, J., Jaunsen, A. O., Letawe, G., & Meylan, G., 2002, A&A, 383, 71
- Chabrier, G., 2003, PASP, 115, 763
- Chartas, G., Gupta, V., Garmire, G., Jones, C., Falco, E. E., Shapiro, I. I., & Tavecchio, F., 2002, ApJ, 565, 96
- Chartas, G., Dai, X., & Garmire, G. P., 2004, Carnegie Observatories Astrophysics Series, Volume 2, *Measuring and Modeling the Universe*, <http://www.ociv.edu/ociv/symposia/series/symposium2/proceedings.html>
- Charlot, S. & Fall, S. M., ApJ, 539, 718
- Chen, J., Rozo, E., Delal, N., Taylor, J. E., 2007, ApJ, 659, 52
- Chiba, M., Minezaki, T., Nashikawa, N., Kataza, H., Inoue, K. T., 2005, ApJ, 627, 61
- Cohn, J. D., Kochanek, C. S., McLeod, B. A., & Keeton, C. R., 2001, ApJ, 554, 1216
- Coles, J., 2008, ApJ, 679, 17
- Colley, W., et al., 2003, ApJ, 587, 71
- Conner, S. R., Lehár, J., & Burke, B. F., 1992, ApJ, 387, L61
- Conroy, C., Gunn, J. E., & White, M., 2009, ApJ, 699, 486
- Cooray, A., & Sheth, R., 2002, Phys. Res., 372, 1
- Dalal, N., & Kochanek, C. S., 2002, ApJ, 572, 25
- Davis, T. M., et al., 2007, ApJ, 666, 715
- Dobler, G. & Keeton, C. R., MNRAS, 365, 1243
- Dunkley, J., et al., 2008, ApJS, 180, 306
- Eisenstein, D. J., 2001, AJ, 122, 2267
- Elíasdóttir, Á., Hjorth, J., Toft, S., Burud, I., & Paraficz, D., ApJS, 166, 443
- Falco, E. E., Gorenstein, M. V., & Shapiro, I. I., 1985, ApJ, 289, L1
- Falco, E. E., Impey, C. D., Kochanek, C. S., Lehiř, J., McLeod, B. A., Rix, H.-W., Keeton, C. R., Muñoz, J. A., & Peng, C. Y., 1999, ApJ, 523, 617
- Fassnacht, C. D., & Lubin, L. M., 2002, AJ, 123, 627
- Fassnacht, C. D., Xanthopoulos, E., Koopmans, L. V. E., & Rusin, D., 2002, ApJ, 581, 823
- Fassnacht, C. D., Gal, R. R., Lubin, L. M., McKean, J. P., Squires, G. K., & Readhead, A. C. S., 2006, ApJ, 642, 30
- Fassnacht, C. D., Kocevski, D. D., Auger, M. W., Lubin, L. M., Neureuther, J. L., Jeltama, T. E., Mulchaey, J. S., & McKean, J. P., 2008, ApJ, 681, 1017
- Fischer, P., Bernstein, G., Rhee, G., & Tyson, J. A., 1997, AJ, 113, 521
- Freedman, W. L., et al., 2001, ApJ, 553, 47
- Fruchter, A. S., & Hook, R. N., 2002, PASP, 114, 144
- Garrett, M. A., Calder, R. J., Porcas, R. W., King, L. J., Walsh, D., & Wilkinson, P. N., 1994, MNRAS, 270, 457
- Gavazzi, R., Treu, T., Rhoads, J. D., Koopmans, L. V. E., Bolton, A. S., Burles, S., Massey, R. J., & Moustakas, L. A., 2007, ApJ, 667, 176
- Gavazzi, R., Treu, T., Koopmans, L. V. E., Bolton, A. S., Moustakas, L. A., Burles, S., & Marshall, P. J., 2008, ApJ, 677, 1046
- Gelman, A., Carlin, J. B., Stern, H. S., & Rubin, D. B., 1995, Bayesian Data Analysis (New York: Chapman & Hall/CRC)
- Gerhard, O., Kronawitter, A., Saglia, R. B., & Bender, R., 2001, AJ, 121, 1936
- Goicoechea, Gil-Merino, R., & Ullán, A., 2005, MNRAS, 360, L60
- Goicoechea, L. J., Shalyapin, V. N., Koptelova, E., Gil-Merino, R., Zheleznyak, A. P., & Ullán, A., 2008, New Astronomy, 13, 182
- Gorenstein, M. V., Cohen, N. L., Shapiro, I. I., Rogers, A. E. E., Bonometti, R. J., Falco, E. E., Bartel, N., & Marcaide, J. M., 1988b, ApJ, 334, 42
- Gorenstein, M. V., Shapiro, I. I., & Falco, E. E., 1988a, ApJ, 327, 693
- Grillo, C., Gobat, R., Lombardi, M., & Rosati, P., 2009, A&A, 501, 461
- Grogin, N. A., & Narayan, R., 1996, ApJ, 464, 92; erratum, 1996, ApJ, 473, 570
- Haario, H., Saksman, E., & Tamminen, J., 2001, Bernoulli, 7, 223
- Haarsma, D. B., Hewitt, J. N., Lehar, J., & Burke, B. F., 1999, ApJ, 510, 64
- Hjorth, J., Burud, I., Jaunsen, A. O., Schechter, P. L., Kneib, J. P., Andersen, M. I., Korhonen, H., Clasen, J. W., Kaas, A. A., Østensen, R., Pelt, J., & Pijpers, F. P., 2002, ApJ, 572, L11
- Jakobsson, P., Hjorth, J., Burud, I., Letawe, G., Lidman, C., & Courbin, F., 2005, A&A, 431, 103
- Jiang, G. & Kochanek, C. S., 2007, ApJ, 671, 1568
- Keeton, C. R. & Kochanek, C. S., 1997, ApJ, 487, 42
- Keeton, C. R., Kochanek, C. S., & Seljak, U., 1997, ApJ, 482, 604
- Keeton, C. R. & Kochanek, C. S., 1998, ApJ, 495, 157
- Keeton, C. R., Falco, E. E., Impey, C. D., Kochanek, C. S., Lehiř, J., McLeod, B. A., Rix, H.-W., Muñoz, J. A., & Peng, C. Y., 2000, ApJ, 542, 74
- Keeton, C. R., 2001, preprint arXiv:astro-ph/0102340
- Keeton, C. R., & Zabludoff, A. I., 2004, ApJ, 612, 600
- Kelson, D. D., Zabludoff, A. I., Williams, K. A., Trager, S. C., Mulchaey, J. S., & Bolte, M., 2002, ApJ, 576, 720
- Kochanek, C. S., Blandford, R. D., Lawrence, C. R., & Narayan, R., 1989, MNRAS, 238, 43
- Kochanek, C. S., 1991, ApJ, 382, 58
- Kochanek, C. S., 1995, ApJ, 445, 559
- Kochanek, C. S., Keeton, C. R., & McLeod, B. A., 2001, ApJ, 547, 50
- Kochanek, C. S., 2002, ApJ, 578, 25
- Kochanek, C. S., 2004, preprint arXiv:astro-ph/0407232
- Kochanek, C. S., Morgan, N. D., Falco, E. E., McLeod, B. A., Winn, J. N., Dembicky, J., & Ketzbeck, B., 2006, ApJ, 640, 47
- Komatsu, E., et al. 2008, ApJS, 180, 330
- Koopmans, L. V. E., de Bruyn, A. G., Xanthopoulos, E., & Fassnacht, C. D., 2000, A&A, 356, 391
- Koopmans, L. V. E., Treu, T., Fassnacht, C. D., Blandford, R. D., & Surpi, G., 2003, ApJ, 599, 70
- Koopmans, L. V. E., Treu, T., Bolton, A. S., Burles, S., & Moustakas, L. A., 2006, ApJ, 649, 599
- Kundic, T., et al., 1997, ApJ, 482, 75
- Lagattuta, D. J., Fassnacht, C. D., Auger, M. W., Bradac, M., Marshall, P. J., Treu, T., Gavazzi, R., & Schrabback, T., 2009, BAAS, 41, 445
- Lartillot, N. & Phillippe, H., 2006, Systematic Biology, 55, 195
- Lehár, J., Cooke, A. J., Lawrence, C. R., Silber, A. D., & Langston, G. I., 1996, AJ, 111, 1812
- Lehár, J., Burke, B. F., Conner, S. R., Falco, E. E., Fletcher, A. B., Irwin, M., McMahon, R. G., Muslow, T. W. B., & Schechter, P. L., 1997, AJ, 114, 48
- Liddle, A. R., 2007, MNRAS, 377, L74
- Lidman, C., Courbin, F., Meylan, G., Broadhurst, T., Frye, B., & Welch, W. J. W., 1999, ApJ, 514, L57
- Lovell, J. E. J., Jauncey, D. L., Reynolds, J. E., Wieringa, M. H., King, E. A., 1998, ApJ, 508, L51
- Macciò, A. V., Dutton, A. A., van den Bosch, F., Moore, B., Potter, D., & Stadel, J., MNRAS, 378, 55
- MacLeod, C. L., Kochanek, C. S., & Agol, E., 2009, ApJ, 699, 1578
- Macri, L. M., Stanek, K. Z., Bersier, D., Greenhill, L. J., & Reid, M. J., 2006, ApJ, 652, 1133
- Mainini, R., Macciò, A. V., Bonometto, S. A., & Klypin, A., 2003, ApJ, 599, 24
- Marshall, P. J., Hobson, M. P., & Slosar, A., 2003, MNRAS, 346, 489
- Mandelbaum, R., van de Ven, G., & Keeton, C. R., 2009, MNRAS, 398, 635
- Mao, S. & Schneider, P., 1998, MNRAS, 295, 587
- Maraston, C., 2005, MNRAS, 362, 799
- Maraston, C., Strömbäck, G., Thomas, D. A., Wake, D. A., & Nichol, R. C., 2009, MNRAS, 394, L104
- Metcalf, R. B. & Madau, P., 2001, ApJ, 563, 9
- Myers, S. T., et al., 1995, ApJ, 447, L5
- Momcheva, I., Williams, K., Keeton, C., & Zabludoff, A., 2006, ApJ, 641, 169

- Nakajima, R., Bernstein, G., Fadely, R., Keeton, C.R., & Schrabback, T., 2009, *ApJ*, 697, 1793
- Navarro, J. F., Frenk, C. S., & White, S. D. M., 1997, *ApJ*, 462, 563
- Oguri, M., 2007, *ApJ*, 660, 1
- Oscosz, A., Alcalde, D., Serra-Ricart, M., Mediavilla, E., Abajas, C., Barrena, R., Licandro, J., Motta, V., & Mu oz, J. A., 2001, *ApJ*, 552, 81
- Paraficz, D., Hjorth, J., & Elfasd ttir,  ., 2009, *A&A*, 499, 395
- Patnaik, A. R., Narasimha, D., 2001, *MNRAS*, 326, 1403
- Poindexter, S., Morgan, N., Kochanek, C. S., & Falco, E. E., 2007, *ApJ*, 660, 146
- Rapetti, D., Allen, S. W., Amin, M. A., & Blandford, R. D., 2007, *MNRAS*, 375, 1510
- Reiss, A. G., Macri, L., Casertano, S., Sosey, M., Lampeitl, H., Ferguson, H. C., Filippenko, A. V., Jha, S. W., Li, W., Chornock, R., & Sarkar, D., 2009, *ApJ*, 699, 539
- Roberts, G. O., Gelman, A., & Gilks, W. R., 1997, *Annals of Applied Probability*, 7, 110
- Roberts, G. O. & Rosenthal, J. S., 2001, *Statistical Science*, 16, 351
- Romanowsky, A. & Kochanek, C. S., 1999, *ApJ*, 516, 18
- Rusin, D., Kochanek, C. S., & Keeton, C. R., 2003, *ApJ*, 595, 29
- Rusin, D., & Kochanek, C. S., 2005, *ApJ*, 623, 666
- Saha, P., Coles, J., Macci , A. V., & Williams, L. L. R., 2006, *ApJ*, 650, L17
- Saha, P., & Williams, L. L. R., 2006, *ApJ*, 653, 936
- Schawinski, K., Thomas, D., Sarzi, M., Maraston, C., Kaviraj, S., Joo, S.-J., Yi, S. K., & Silk, J., *MNRAS*, 2007, 382, 1415
- Schild, R. E. & Cholfin, B., 1986, *ApJ*, 300, 209
- Schlegel, D. J., Finkbeiner, D. P., & Davis, M., 1998, *ApJ*, 500, 525
- Schneider, P., Ehlers, J., & Falco, E. E., 1992, *Gravitational Lenses* (New York: Springer)
- Schramm, T., 1990, *A&A*, 231, 19
- Schwarz, G., 1978, *Ann. Stat.*, 6, 461
- Springel, V., et al., 2005, *Nature*, 435, 629
- Suyu, S. H., Marshall, P. J., Blandford, R. D., Fassnacht, C. D., Koopmans, L. V. E., McKean, J. P., & Treu, T., 2008, *ApJ*, 691, 277
- Suyu, S. H., Marshall, P. J., Auger, M. W., Hilbert, S., Blandford, R. D., Koopmans, L. V. E., Fassnacht, C. D., & Treu, T., 2009, preprint arXiv:0910.2773
- Tonry, J.L. & Franx, M., 1999, *ApJ*, 515, 512
- Treu, T. & Koopmans, L. V. E., 2002, *MNRAS*, 337, L6
- Treu, T., Koopmans, L. V., Bolton, A. S., Burles, S., & Moustakas, L. A., 2006, *ApJ*, 640, 662
- Trotter, C. S., Winn, J. N., & Hewitt, J. N., 2000, *ApJ*, 535, 671
- van de Ven, G., Mandelbaum, R., & Keeton, C. R., 2009, *MNRAS*, 398, 607
- Vuissoz, C., Courbin, F., Sluse, D., Meylan, G., Ibrahimov, M., Asfandiyarov, I., Stoops, E., Eigenbrod, A., Le Guillou, L., van Winckel, & H., Magain, P., 2007, *A&A*, 464, 845
- Wake, D. A., et al., 2006, *MNRAS*, 372, 537
- Walsh, D., Carswell, R. F., & Weymann, R. J., 1979, *Nature*, 279, 381
- Williams, K. A., Momcheva, I., Keeton, C. R., Zabludoff, A. I., & Leh r, J., 2006, *ApJ*, 646, 85
- Williams, L. L. R. & Saha, P., 2000, *ApJ*, 119, 439
- Winn, J. N., Kochanek, C. S., McLeod, B. A., Falco, E. E., Impey, C. D., & Rix, H.-W., 575, 103
- Wucknitz, O., Biggs, A. D., & Browne, I. W. A., 2004, *MNRAS*, 349, 14
- York, T., Jackson, N., Browne, I. W. A., Wucknitz, O., & Skelton, J. E., 2005, *MNRAS*, 357, 124

TABLE 1
LENS GALAXY PHOTOMETRY

Filter	Total Counts	m_{AB}	Zeropoint, AB ¹
F606W	3328.6	18.809 ± 0.061	27.614
F814W	5372.9	17.743 ± 0.065	27.068

¹ Quoted zeropoints differ from standard values as we must correct for a plate scale change from 0.05'' to 0.03'' pixels

TABLE 2
MODELING CONSTRAINTS

Feature	Position (") ¹	Symbol in Figure 3
G1	(0, 0) ± 0.00001	—
Quasar A	(1.408, 5.034) ± 0.03	Green Plus
Quasar B	(0.182, -1.018) ± 0.03	Green Plus
Jet A5	(1.392, 5.080) ± 0.03	—
Jet B5	(0.164, -0.962) ± 0.03	—
IA	(2.878, 3.453) ± 0.05	Red Circle
IB	(-1.362, -0.043) ± 0.05	Red Circle
IIA	(2.666, 3.634) ± 0.05	Blue Circle
IIB	(-1.457, -0.075) ± 0.05	Blue Circle
IIIA	(2.395, 3.694) ± 0.05	Cyan Circle
IIIB	(-1.682, -0.026) ± 0.05	Cyan Circle
IVA	(0.021, -2.532) ± 0.03	Green Diamond
IVB	(0.512, -2.386) ± 0.03	Green Diamond
VA	(2.111, 3.664) ± 0.05	Red Diamond
VB	(-0.768, -2.640) ± 0.05	Red Diamond
VIA	(1.875, 3.488) ± 0.12	Blue Diamond
VIB	(-1.128, -2.777) ± 0.05	Blue Diamond
VIC	(1.523, -1.634) ± 0.05	Blue Diamond
VIIA	(1.875, 3.488) ± 0.12	—
VIIIB	(-1.065, -2.786) ± 0.05	—
VIII	(1.489, -1.688) ± 0.05	—
VIIIA	(2.280, 3.391) ± 0.09	Magenta Diamond
VIIIB	(-0.454, -2.873) ± 0.09	Magenta Diamond
IXA	(-2.003, -2.435) ± 0.05	Cyan Diamond
IXB	(1.293, 3.611) ± 0.05	Cyan Diamond
XA	(-1.708, -1.878) ± 0.08	Yellow Circle
XB	(-2.181, -0.551) ± 0.08	Yellow Circle
XIA	(-2.070, -1.252) ± 0.08	Magenta Circle
XIB	(-2.112, -1.053) ± 0.08	Magenta Circle
XIIA	(-2.745, -0.516) ± 0.08	Green Circle
XIIB	(-2.781, -0.699) ± 0.08	Green Circle

NOTE. — New features are indicated with Roman numerals

¹ Written as (x, y) where x is West and y is North.

TABLE 3
MODEL PARAMETERS

Parameter	Label
Stellar mass to light ratio	Υ_{F606W}
Halo ellipticity	e
Position angle	PA
Shear angle	θ_γ
Core radius (α models)	a
Scale radius (NFW models)	r_s
σ angle	θ_σ
δ angle	θ_δ
Halo mass normalization	b_d
External Shear	γ
3 rd order term	σ
3 rd order term	δ

NOTE. — Power law α models use a core radius a , while NFW models use a scale radius r_s .

TABLE 4
SPS MODEL PARAMETERS

Parameter	Prior	FSPS	Maraston SPS
Formation redshift, z_f	0.361 – 1089	✓	✓
SFR e-folding time, τ	$0 - \infty$	✓	✓
Constant SFR, C	0 – 1	✓	✓
Dust around young stars, τ_1	$0 - \infty$	✓	✓
Diffuse dust ¹ , τ_2	$P \propto e^{-1.086\tau_2}$	✓	✓
Fraction of blue HB stars ² , f_{BHB}	0 – 0.5	✓	–
Specific frequency of blue stragglers ² , S_{BS}	0 – 10	✓	–
Shift in $\log(L_{bol})$ along the TP-AGB ² , Δ_L	–0.4 – 0.4	✓	–
Shift in $\log(T_{eff})$ along the TP-AGB ² , Δ_T	–0.2 – 0.2	✓	–

¹ We use a exponential prior on the diffuse dust content of the form $e^{-A_{F606W}/1.0mag}$

² See Conroy et al. (2009) for details

TABLE 5
MODEL RESULTS: HST-ACS DATA

Parameter	Median model values with 68% CL (95% CL) uncertainties			
	NFW	$\alpha = 0.5$	$\alpha = 1.0$	$\alpha = 1.5$
Υ_{F606W}	$7.7^{+3.3}_{-2.7}$ (+4.9)	$5.4^{+2.5}_{-0.6}$ (+3.9)	$7.4^{+1.5}_{-1.8}$ (+3.0)	$8.6^{+1.1}_{-1.5}$ (+2.2)
b_d (")	$0.097^{+0.01}_{-0.022}$ (+0.118)	$6.3^{+1.6}_{-1.4}$ (+2.6)	$4.4^{+1.3}_{-0.8}$ (+2.6)	$3.1^{+0.6}_{-0.5}$ (+1.0)
e	$0.46^{+0.19}_{-0.19}$ (+0.30)	$0.31^{+0.14}_{-0.13}$ (+0.22)	$0.40^{+0.12}_{-0.14}$ (+0.24)	$0.44^{+0.15}_{-0.11}$ (+0.24)
θ_e (°)	70^{+7}_{-6} (+12)	72^{+9}_{-10} (+15)	71^{+9}_{-7} (+14)	72^{+9}_{-6} (+14)
γ ($\times 10^2$)	$7.8^{+3.0}_{-2.7}$ (+5.0)	$7.6^{+2.1}_{-2.8}$ (+3.5)	$7.8^{+3.1}_{-2.5}$ (+5.2)	$7.5^{+4.2}_{-3.4}$ (+5.8)
θ_γ (°)	52^{+11}_{-15} (+15)	51^{+11}_{-13} (+16)	51^{+10}_{-14} (+15)	42^{+16}_{-19} (+26)
a (")	–	$5.7^{+1.2}_{-1.1}$ (+2.0)	$4.0^{+1.0}_{-0.9}$ (+1.7)	$1.8^{+0.5}_{-0.7}$ (+1.0)
σ ($\times 10^3$)	$2.6^{+1.7}_{-1.3}$ (+2.7)	$1.9^{+1.1}_{-0.9}$ (+1.8)	$1.8^{+1.3}_{-0.9}$ (+2.0)	$1.9^{+1.0}_{-1.4}$ (+1.6)
θ_σ (°)	335^{+5}_{-32} (+14)	210^{+46}_{-19} (+95)	233^{+61}_{-184} (+106)	266^{+51}_{-197} (+85)
δ ($\times 10^3$)	$2.8^{+1.8}_{-1.1}$ (+3.0)	$2.6^{+1.0}_{-1.0}$ (+1.8)	$2.4^{+1.5}_{-1.0}$ (+2.6)	$3.3^{+0.9}_{-1.4}$ (+1.9)
θ_δ (°)	68^{+9}_{-17} (+17)	61^{+11}_{-13} (+18)	59^{+17}_{-13} (+21)	62^{+10}_{-5} (+15)
f_B/f_A	$0.55^{+0.10}_{-0.06}$ (+0.22)	$0.53^{+0.05}_{-0.05}$ (+0.09)	$0.50^{+0.06}_{-0.04}$ (+0.09)	$0.51^{+0.07}_{-0.04}$ (+0.12)
$\kappa_{s,30''}$	$0.12^{+0.07}_{-0.02}$ (+0.10)	$0.15^{+0.07}_{-0.05}$ (+0.13)	$0.21^{+0.07}_{-0.07}$ (+0.11)	$0.27^{+0.04}_{-0.04}$ (+0.07)
H_0	$89.4^{+16.8}_{-13.7}$ (+27.3)	$75.3^{+13.8}_{-10.0}$ (+23.4)	$84.4^{+11.1}_{-11.3}$ (+18.3)	$89.9^{+10.1}_{-10.0}$ (+17.0)
$\min(\chi^2_{reduced})$	0.38	0.91	0.90	0.58
P_{rel}	0.014	0.575	1.000	0.114

TABLE 6
MODEL RESULTS: HST-ACS DATA + MARASTON SPS MODELS

Parameter	Median model values with 68% CL (95% CL) uncertainties			
	NFW	$\alpha = 0.5$	$\alpha = 1.0$	$\alpha = 1.5$
Υ_{F606W}	$5.7^{+1.2}_{-1.2}$ (+1.9)	$5.3^{+1.1}_{-0.9}$ (+2.9)	$6.5^{+1.0}_{-1.8}$ (+1.6)	$6.9^{+0.9}_{-1.0}$ (+1.4)
b_d (")	$0.118^{+0.028}_{-0.018}$ (+0.107)	$6.4^{+1.5}_{-1.2}$ (+2.5)	$5.0^{+1.3}_{-2.0}$ (+2.3)	$3.5^{+0.5}_{-0.5}$ (+0.9)
e	$0.34^{+0.09}_{-0.09}$ (+0.14)	$0.30^{+0.6}_{-0.11}$ (+0.16)	$0.32^{+0.10}_{-0.14}$ (+0.115)	$0.34^{+0.08}_{-0.08}$ (+0.11)
θ_e (°)	70^{+8}_{-8} (+13)	73^{+8}_{-10} (+13)	72^{+9}_{-9} (+13)	76^{+8}_{-6} (+12)
γ ($\times 10^2$)	$8.6^{+3.0}_{-2.9}$ (+4.5)	$7.7^{+2.8}_{-2.1}$ (+4.1)	$8.2^{+2.8}_{-2.5}$ (+5.1)	$9.8^{+2.9}_{-3.4}$ (+6.1)
θ_γ (°)	55^{+8}_{-12} (+13)	51^{+10}_{-11} (+16)	52^{+9}_{-12} (+15)	49^{+7}_{-9} (+15)
a (")	–	$5.8^{+1.1}_{-1.1}$ (+1.9)	$4.0^{+1.0}_{-0.9}$ (+1.7)	$1.4^{+0.5}_{-0.5}$ (+0.8)
σ ($\times 10^3$)	$2.0^{+1.5}_{-1.1}$ (+2.5)	$1.9^{+1.1}_{-0.9}$ (+1.7)	$1.8^{+1.4}_{-0.9}$ (+2.0)	$1.9^{+1.0}_{-1.2}$ (+1.6)
θ_σ (°)	235^{+39}_{-95} (+80)	211^{+39}_{-119} (+81)	228^{+36}_{-96} (+82)	229^{+26}_{-70} (+82)
δ ($\times 10^3$)	$2.8^{+1.4}_{-1.4}$ (+2.4)	$2.5^{+1.1}_{-0.9}$ (+1.8)	$2.4^{+1.1}_{-1.2}$ (+1.9)	$3.0^{+1.2}_{-1.3}$ (+2.8)
θ_δ (°)	68^{+10}_{-16} (+18)	61^{+11}_{-12} (+17)	60^{+16}_{-14} (+23)	67^{+10}_{-14} (+19)
f_B/f_A	$0.61^{+0.08}_{-0.06}$ (+0.18)	$0.53^{+0.05}_{-0.05}$ (+0.09)	$0.53^{+0.05}_{-0.06}$ (+0.08)	$0.58^{+0.07}_{-0.06}$ (+0.11)
$\kappa_{s,30''}$	$0.17^{+0.03}_{-0.05}$ (+0.05)	$0.13^{+0.03}_{-0.02}$ (+0.04)	$0.16^{+0.02}_{-0.03}$ (+0.04)	$0.23^{+0.01}_{-0.02}$ (+0.02)
H_0	$82.9^{+6.9}_{-7.3}$ (+12.2)	$73.7^{+7.6}_{-7.6}$ (+12.4)	$78.4^{+6.6}_{-7.6}$ (+10.2)	$82.2^{+5.7}_{-6.2}$ (+8.7)
$\min(\chi^2_{reduced})$	0.57	0.99	0.98	0.83
P_{rel}	0.010	0.814	1.000	0.053

TABLE 7
MODEL RESULTS: HST-ACS DATA + H_0 PRIORS

Parameter	Median model values with 68% CL (95% CL) uncertainties							
	NFW	$\alpha = 0.5$		$\alpha = 1.0$		$\alpha = 1.5$		
Υ_{F606W}	$4.3^{+0.7}_{-1.2}$	$3.6^{+0.2}_{-0.6}$	$5.5^{+0.5}_{-0.5}$	$5.1^{+0.2}_{-0.3}$	$5.6^{+1.3}_{-0.6}$	$5.0^{+0.2}_{-0.3}$	$5.8^{+0.5}_{-0.5}$	$5.7^{+0.3}_{-0.4}$
b_d (")	$0.135^{+0.028}_{-0.018}$	$0.144^{+0.037}_{-0.011}$	$6.3^{+1.3}_{-1.0}$	$6.7^{+1.2}_{-1.1}$	$5.5^{+1.1}_{-1.1}$	$5.6^{+1.2}_{-1.5}$	$4.1^{+0.3}_{-0.5}$	$4.1^{+0.4}_{-0.5}$
e	$0.25^{+0.06}_{-0.07}$	$0.19^{+0.05}_{-0.04}$	$0.31^{+0.07}_{-0.10}$	$0.26^{+0.07}_{-0.09}$	$0.28^{+0.08}_{-0.07}$	$0.21^{+0.08}_{-0.06}$	$0.25^{+0.06}_{-0.07}$	$25^{+0.07}_{-0.06}$
θ_e (°)	69^{+12}_{-9}	69^{+11}_{-11}	74^{+9}_{-10}	74^{+9}_{-10}	72^{+9}_{-9}	72^{+8}_{-8}	77^{+9}_{-10}	77^{+7}_{-8}
γ ($\times 10^2$)	$9.6^{+3.0}_{-2.6}$	$10.0^{+2.0}_{-2.0}$	$7.6^{+2.7}_{-1.9}$	$7.8^{+2.4}_{-2.0}$	$8.2^{+2.5}_{-2.6}$	$8.6^{+2.2}_{-2.6}$	$11.0^{+2.3}_{-3.0}$	$11.0^{+3.0}_{-2.2}$
θ_γ (°)	57^{+6}_{-11}	58^{+6}_{-8}	50^{+11}_{-14}	52^{+8}_{-14}	52^{+10}_{-12}	56^{+5}_{-10}	51^{+16}_{-8}	51^{+10}_{-7}
a (")	—	—	$5.8^{+1.1}_{-1.0}$	$5.9^{+1.1}_{-1.0}$	$4.2^{+1.0}_{-0.7}$	$4.1^{+0.8}_{-0.6}$	$1.3^{+0.6}_{-0.7}$	$1.3^{+0.5}_{-0.5}$
σ ($\times 10^3$)	$2.5^{+1.6}_{-1.1}$	$3.3^{+1.2}_{-1.4}$	$1.9^{+1.1}_{-1.0}$	$2.1^{+0.9}_{-1.1}$	$1.9^{+1.4}_{-1.1}$	$2.0^{+1.3}_{-1.0}$	$2.2^{+0.9}_{-0.9}$	$2.2^{+0.9}_{-0.9}$
θ_σ (°)	213^{+23}_{-42}	211^{+10}_{-36}	215^{+45}_{-27}	215^{+30}_{-114}	221^{+24}_{-74}	220^{+21}_{-26}	180^{+47}_{-66}	185^{+39}_{-60}
δ ($\times 10^3$)	$2.8^{+1.1}_{-1.5}$	$2.4^{+1.4}_{-1.2}$	$2.3^{+1.3}_{-0.7}$	$2.5^{+1.1}_{-1.6}$	$2.3^{+1.1}_{-1.5}$	$2.3^{+1.0}_{-1.3}$	$3.8^{+2.0}_{-1.3}$	$3.8^{+1.1}_{-1.0}$
θ_δ (°)	68^{+10}_{-16}	70^{+19}_{-28}	61^{+11}_{-12}	62^{+11}_{-16}	63^{+15}_{-16}	63^{+17}_{-16}	69^{+4}_{-10}	68^{+4}_{-8}
f_B/f_A	$0.66^{+0.09}_{-0.06}$	$73^{+0.22}_{-0.07}$	$0.52^{+0.05}_{-0.04}$	$0.53^{+0.05}_{-0.04}$	$0.53^{+0.05}_{-0.04}$	$0.55^{+0.05}_{-0.03}$	$0.61^{+0.04}_{-0.05}$	$0.60^{+0.05}_{-0.04}$
$\kappa_{s,30''}$	$0.17^{+0.04}_{-0.05}$	$0.17^{+0.03}_{-0.04}$	$0.13^{+0.02}_{-0.02}$	$0.13^{+0.02}_{-0.02}$	$0.17^{+0.02}_{-0.02}$	$0.17^{+0.02}_{-0.02}$	$0.24^{+0.01}_{-0.01}$	$0.24^{+0.01}_{-0.01}$
P_{rel}	0.007	0.003	1.000	1.000	0.869	0.565	0.006	0.000

NOTE. — Columns on the left use $H_0 = 74.2 \pm 3.6 \text{ km s}^{-1} \text{ Mpc}^{-1}$ from Riess et al. (2009) while columns on the right use $H_0 = 70.5 \pm 1.3 \text{ km s}^{-1} \text{ Mpc}^{-1}$ from Komatsu et al. (2008).